Engineering a Novel Device to Implement Afterload on Human Stem Cell–Derived Cardiac Tissues

Shiv Bhandari

A thesis

submitted in partial fulfillment of the

requirements for the degree of

MASTER OF SCIENCE IN BIOENGINEERING

University of Washington

2015

Committee:

Charles E. Murry, Chair

Nathan J. Sniadecki

Program Authorized to Offer Degree:

Department of Bioengineering

University of Washington

Abstract

Engineering a Novel Device to Implement Afterload on
Human Stem Cell–Derived Cardiac Tissues

Shiv Bhandari

Chair of the Supervisory Committee:
Dr. Charles E. Murry, MD, PhD
Departments of Pathology, Bioengineering, and Medicine

Cardiac tissue engineering is a promising approach towards regenerating healthy myocardium and restoring the function of infarcted hearts. Using human embryonic stem cell (hESC) derived cardiomyocytes seeded in a collagen or fibrin scaffold, we have previously been able to generate engineered heart tissues (EHTs) that spontaneously contract, but with an amplitude that is far inferior to that of the native myocardium. In order to improve tissue maturation, our goal is to exercise and strengthen EHTs by applying the same mechanical load that the left ventricle faces during contractions—cardiac afterload. My investigation focuses on designing, building, and optimizing a device to apply cardiac afterload on hESC-EHTs. The afterload system involves anchoring tissues between two flexible posts made from polydimethylsiloxane: a rigid post that positions the tissue, and a flexible post containing a

neodymium cube magnet that can be manipulated by an external bar magnet. The device is capable of providing a tunable resistance to tissue contractions that models the levels of afterload occurring in the developing heart at particular time points. We tested the load and rate dependency of afterload conditioning on constructs and found that tissues treated with afterload displayed 12.5-fold higher active stresses compared to unloaded controls, and were comparable with tissues undergoing isometric contractions (i.e. infinite afterload). The afterload device has provided us with an insight into the role of mechanical stimuli in promoting the maturation of hESC-EHTs. Our findings suggest that both static loads at 2 and 4 kPa, and steady increases in resistive loads from 0 to 8 kPa do not promote tissue contractility compared with isometric controls. Future work includes testing different static and dynamic loading regimes to identify the optimum level of afterload to promote construct maturation. In summary, we were able to engineer a novel system that applies physiological levels of afterload onto hESC-EHTs. With this new system, we performed the first studies to investigate the role of afterload conditioning in promoting the maturation of hESC-EHTs.

TABLE OF CONTENTS

List of Figures

List of Tables

ACKNOWLEDGEMENTS

I would first and foremost like to thank my advisor, Chuck Murry, for giving me the opportunity to continue researching and bring my undergraduate project to fruition as a master's student. It has been a privilege to train to be a bioengineer under Chuck, who has provided me with invaluable mentorship every step of the way. It has been an honor to be a part of the Murry Lab team, and I would like to thank and recognize each team member in lab who would stop at a moment's notice to help me along with my investigation: Astrid Breitbart, Danny Burnham, Johannes Bargehr, Likai Chen, Kareen Coulombe, Khue Dao, Clayton Friedman, James Fugate, Peter Hofsteen, Sonal Jain, Jasmine Kim, Amy Martinson, Veronica Muskheli, Lil Pabon, Nathan Palpant, Hans Reinecki, Meredith Roberts, Jialing Ruan, Mark Saiget, Cody Schopf, Nick Strash, Akiko Tsuchida, Melissa Walzer, Florian Weinberger, Isa Werny, Luz Linares, Daniel Yang, Xiulan Yang, and Becky Zaunbrecher. I would like to thank my supervisory committee member, Nate Sniadecki, for pointing me in the right direction whenever I needed guidance on my project. A great portion of my investigation would not have been possible without the help from Kevin Bielawski, Andrea Leonard, and Marita Rodriguez from the Sniadecki team, who worked with me for hours and days on end as we solved some of the most difficult issues with the project. I would also like to thank Jordan Klaiman, Maria Razumova, and Fareed Moussavi-Harami from the Regnier Lab who not only helped me acquire critical data for my experiments, but also gave me sound advice whenever I was having trouble with my investigation.

It has been a highlight to have worked with and fostered relationships with these brilliant researchers who have made my journey as a master's student an invaluable experience.

Introduction

Cardiovascular Disease

Cardiovascular disease (CVD) is presently the leading cause of death worldwide, accounting for over 17 million deaths each year and $863 billion in direct and indirect costs. Unfortunately, these figures are on the rise: by 2030, CVD is expected to result in over 23.6 million deaths globally, creating economic burden of over $1.04 trillion. In the United States, CVD has remained the most common cause of mortality for over seventy-five years. In 2010 alone, over 375,000 Americans died from CVD, amounting to over $320.1 billion[1–3] in healthcare costs. A genetic predisposition elevates the risk for CVD, however the growing prevalence is also due to environmental factors that include obesity, physical inactivity, and diabetes[4–6]. The enormous burden of CVD on people within the United States and around the world emphasizes the pressing need to find a cure.

CVDs encompass a broad range of ailments that pertain to the heart, such as heart valve disorders, arrhythmias, strokes, and myocardial infarctions (MI). A MI occurs when a coronary artery becomes occluded from plaque buildup, thereby preventing blood from accessing and providing nourishment downstream into the myocardium. If the occlusion persists for more than 20 minutes, irreversible damage to the cardiomyocytes can occur resulting in myocardial necrosis[7]. Unlike other animals that can regenerate healthy heart tissue, such as salamanders and zebrafish[8], human beings have a very low cardiac regenerative capacity. Less than 1% of human cardiomyocytes turn over annually, thereby taking a lifetime to renew only 50% of the cardiomyocytes in an adult human heart[9]. As such, the necrotic tissue is replaced by non-contractile scar tissue that initiates remodeling of the left ventricle. The resulting dilation of the

chamber and compensatory pathological hypertrophy of the non-infarcted myocardium leads to a reduction in overall cardiac output[10,11].

There are several treatment options available for patients who have survived a MI. If cardiac output has severely decreased, a mechanical heart pump such as a left ventricular assist device can be surgically implanted to facilitate pumping. If the patient is at end-stage heart failure, a complete heart transplant might be necessary[12,13]. However, there are approximately 25,000 patients who would benefit from heart transplants currently in the United States and only around 2,500 donor hearts available for transplantation each year[14]. None of the current treatment options can reintroduce healthy myocardium within the scarred region of an infarcted heart, prompting researchers to look into cardiac regenerative therapy as a potential cure for heart failure.

Regenerative Medicine

Cardiac regenerative medicine focuses on rebuilding the myocardium using novel techniques such as scar tissue reprogramming, cell-based therapies, and tissue engineering. Scar reprogramming involves targeting fibroblasts within the scar region and transforming them into cardiac progenitors or cardiomyocytes using retroviral delivery of genes that encode cardiac-inducing factors. Scar reprogramming on mouse models have shown successful transformation of fibroblasts into cardiac-like cells, and further investigation on the efficacy of transformation and safety of gene delivery for future clinical application is currently underway[15–17]. Cell transplantation involves delivering cells to the infarct region via direct injection or mobilization via the administration of growth factors. The goals of cell transplantation are to either a) introduce paracrine-mediate effects to induce the growth of native cardiomyocytes or stimulate

endogenous myocardial stem cells, or b) to directly introduce new cardiomyocytes into the infarct region[18,19]. Several studies (including those done at the Murry Lab) have indicated that injection of human pluripotent stem cell-derived cardiomyocytes into animal models can improve systolic function[20–23]. Another big avenue of research in cardiac regenerative medicine is tissue engineering. The idea of tissue engineering is to encapsulate cells within a matrix to form a three dimensional piece of contractile tissue. The choice of matrix can vary among collagen, Matrigel, fibrin, polyglycolic acid (PGA), alginate, polyethylene glycol, and many others. A variety of cell types can be used, including fetal/neonatal rat/mouse myocytes, human umbilical vein endothelial cells (HUVECs), and hiPSC/hESC-derived cardiomyocytes[24]. In order to regenerate healthy heart tissue, the ultimate goal is to surgically implant the human stem cell-derived engineered heart tissue (hSC-EHT) to replace the scar and improve cardiac function.

In order for hSC-EHTs to meet this ambitious goal, they must first overcome several critical barriers to clinical application. The biggest issue is to match the active force produced by the heart. The native myocardium produces active stresses of 20-40 mN/mm^2, over ten-fold greater than the maximum active stresses of 2-0.8 mN/mm^2 generally observed in hESC-derived cardiac constructs[25–28]. Another issue of engineered tissues is the limitation on their size if they do not have a preformed vasculature. Within the body, diffusion of nutrients becomes poor when cells are at distances of >200μm from a vessel[29]. This issue applies towards engineered constructs as well, where cells in the middle of construct may face necrosis if the tissue is too thick[30]. Cardiac muscle is composed of striated and aligned cardiomyocytes that are multinucleated and electrically coupled via gap junctions. Most stem-cell derived cardiac tissues do not exhibit the intricate cellular organization observed in native heart tissue[31]. There are several approaches towards promoting the maturation of stem cell-derived cardiac constructs:

mechanical loading and electrical stimulation[32–36]; treatment with biochemical cues such as adrenergic receptor agonists[37], triiodothyronine[38], insulin-like growth factor I [39], ascorbate[40,41], and microRNAs[42]; mixing cardiomyocytes with supporting cell lines (e.g. stromal cells)[26,43]; and manipulating the extracellular matrix[27,31,44–46] to enhance cardiomyocyte alignment/size, proliferation, gene expression, sarcomere length, and contractility.

Maturation of EHTs via Mechanical Stretch

Several groups have shown that applying mechanical stimulation promotes the maturation of EHTs[32–35]. In an early study, Eschenhagen found that implementing up to 20% cyclic stretch at 1.5Hz on EHTs made with neonatal rat ventricular myocytes (NRVMs) for six days resulted in constructs with parallel arrays of rod-shaped cardiomyocytes, increased cell area, longer myofilaments, increased mitochondrial density, and 3.8-fold increase in active force compared with unstretched controls[32]. Eschenhagen, Zimmermann, and Claycomb also found that applying cyclic stretch on EHTs can improve tissue morphology and gene expression of certain cardiac markers. Ring shaped EHTs made with NRVMs subjected to 10% unidirectional cyclic mechanical stretch at 2 Hz demonstrated improved tissue morphology and contractility, with highly organized sarcomeres, gap junctions, and a developing T-tubular system[33]. In addition, EHTs made with mouse ESC-derived cardiomyocytes subjected to 10% cyclic stretch at 3 Hz for three days resulted in increased expression levels of α-cardiac actin and α-myosin heavy chain (MHC)[34]. It was also found that 5%, 5 Hz cyclic mechanical strain on EHTs made with chicken embryonic ventricular myocytes increased cardiomyocyte proliferation by 20.5% compared with unstretched controls[35]. In 2006, Eschenhagen performed a study where large, circular (1 – 4 mm thick, 14 mm diameter) EHTs derived from NRVMs were implanted over

infarcted regions in immune-suppressed rats. High resolution epicardial mapping revealed that after 28 days the implanted EHTs were electrically coupled to the heart. They also found reduced dilation of the infarcted ventricle and improved systolic wall thickening and fractional area shortening in the infarcted region compared with controls[44].

The focus of our tissue engineering work at the Murry Lab is to identify mechanisms to promote the maturation of hSC-EHTs. There advantages of using human stem cell-derived cardiomyocytes in constructs are 1) a theoretically unlimited stem cell supply[47]; 2) greater access to studying human cardiac development *in vitro*[48]; 3) the option to generate human disease models and study their pathophysiology[49], 4) a more applicable platform for drug screening[50], and 5) a brighter future in clinical applicability of EHTs for cardiac repair[48].

Several groups, including Ruan and Tulloch at the Murry Lab, have demonstrated that mechanical conditioning of EHTs made with either human embryonic stem cells (hESC) or human induced pluripotent stem cells (hiPSC) promotes structural and functional maturation[26,51,43,40]. EHTs subjected to both static and cyclic loading regimes showed a 2-fold increase in cardiomyocyte alignment and improved sarcomere organization. Conditioning EHTs with 5% cyclic stress at 1 Hz for four days increased cardiomyocyte hypertrophy and proliferation, and step-wise increases in strain resulted in greater active forces, producing Frank-Starling stress-strain curves that occur with intact native heart muscle[26]. It was also found that the cyclic loading regime increased active stress (0.28 ± 0.3 mN/mm^2) more than static stress(0.16 ± 0.4 mN/mm^2), and much more then unstressed constructs (0.05 ± 0.01 mN/mm^2) when constructs were measured under a force transducer and stretched to 25% strain[43].

Cardiac Afterload

There are two fundamental forms of mechanical loading that native heart tissue is subject to with each contraction cycle: preload and afterload. Preload corresponds to the extent of myocardial stretch, or tension, prior to a contraction. An intrinsic property of adult cardiomyocytes is that increasing preload results in greater force production, a phenomenon discovered by Otto Frank and Ernest Starling[52]. The Frank-Starling mechanism dictates that increased venous return results in greater filling of the ventricle and thus, an increased preload. This increased stretch results in greater force generation by the myocardium and enables the heart to eject the larger volume of blood. Afterload corresponds to the force against which the ventricles must contract to eject blood into the aorta, i.e. the tension during the contraction. Increasing aortic pressure thereby increases the afterload on the myocardium which can reduce cardiac output and promote pathological hypertrophy to reduce left ventricular end-systolic (LVES) stress in a negative feedback loop[53]. As the myocardium thickens, the compliance of the left ventricle reduces, thereby reducing the amount of filling during diastole[54–56].

It has previously been shown that increasing afterload enhances contractility in newborn lambs[57,58]. In 1994, Jan Baan found that stepwise increases in afterload, carried out by inflating a balloon catheter in the descending thoracic aorta, elevated the slope of the end-systolic pressure-volume relation from 4.44 ± 2.43 kPa/mL to 6.69 ± 2.89 kPa/mL. Their pressure-volume loop traces corresponding to higher afterload has a greater area than the traces corresponding to low afterload, indicating greater work done by the left ventricle when afterload is increased. All together, these data supported the claim that the left ventricle is able to maintain stroke volumes at higher levels of afterload in newborn lambs[58].

On a single cell level, it is possible to implement afterload by attaching cardiomyocytes onto an array of posts that have a known stiffness. In the newborn lab afterload studies, larger occlusions increased vascular resistance, thereby increasing the load against which the left ventricle would contract to eject blood. Likewise, an increase in post stiffness adds to the resistance against which single cardiomyocytes contract, simulating an increased afterload. Rodriguez et al found that an increase post stiffness from 3 kPa (0.029 N/m) to 15 kPa (0.142 N/m) correlated with an increase in active force of NRVMs from 15 nN to 75 nN and an increase in work from 12.5 fJ to 75 fJ [59], in similarity with the increase in cardiac work observed with an increase in afterload in the neonatal lamb studies[58].

The majority of EHT studies that implement mechanical loading focus on stretching the tissues via a static or cyclic regime, i.e. subjecting tissues to cardiac preload. However in 2012, Hirt et al developed a system to implement afterload on EHTs made with NRVMs by casting each tissue onto a pair of large, hollow silicone posts, where post stiffness was increased from 0.95 N/m (controls) to 11.5 N/m by the insertion of a metal brace into the posts[45]. They conditioned their EHTs onto the posts with metal braces (afterload conditioning) for eight days and saw an increase in cardiomyocyte size from 62.3 μm^2 to 80.0 μm^2, but interestingly a reduction in active stress from 4.35 mN/mm^2 to 2.82 mN/mm^2. This finding suggests that if the posts are too stiff, then EHTs cannot maintain cardiac output and thus, active stresses will decrease. Eschenhagen reports that the high post stiffness in their afterload group decreased post deflection with each contraction, suggesting that their afterload treatments resembles a condition of near isometric contractions. The stiffness of the posts in their control group was 12-fold lower and produced greater active stresses. These findings suggest that a resistive load that is too high can impair contractility, and that maintaining a lower resistive load can improve contractility. As

such, the motivation of my investigation is to build a system to dynamically control the amount of resistive load placed on hESC-EHTs to test the hypothesis that afterload conditioning promotes tissue contractile and structural maturation.

Fibrin and Collagen Gels

Fibrin and collagen are the most common biological materials used to engineer cardiac tissues *in vitro*. Collagen is composed of a repeating tripeptide sequence: -glycine-x-y- where y is hydroxyproline, an imino acid that allows for rapid twisting of the helix for improved stability and secretion. Collagen has an average pore diameter of 7.4 ± 1.1 μm and a Young's modulus of 0.5 – 12 kPa, depending on collagen concentration[60]. Collagen is responsible for 25 – 30% of the body's protein content and collagen type I is well suited as a material for cardiac tissue engineering as it constitutes 80% of the total collagen content of the myocardium's extra cellular matrix (ECM)[61]. Fibrin is an ionically cross-linked polymer that is produced at the end of the coagulation cascade when fibrinogen is cleaved by thrombin. Fibrinogen is a 340-kD protein that consist of six chains: 2 Aα chains, 2 Bβ chains, and 2 γ chains. Thrombin is an enzyme that cleaves the A and B peptides from fibrinogen, creating a fibrin monomer that can spontaneously crosslink with other fibrin monomers to form a fibrous array[62]. Fibrin has an average pore diameter of 0.6 ± 0.1 μm, and a Young's modulus of 80 kPa[63] depending on fibrin concentration. Fibrin has several advantages as an ECM for tissue engineering, in that the crosslinking rate can be manipulated by the varying the concentration of thrombin, the elastic modulus can be controlled by controlling the fibrinogen concentration, and the degradation rate can be tuned by varying the concentration of serine protease inhibitors[63–65]. Several groups have reported high active stresses from hESC-EHTs made with a fibrin ECM[31,44,45], including the Zhang group that

achieved a peak active stress of 11.8 mN/mm^2 using hESC-derived cardiomyocytes seeded in fibrin/Matrigel scaffold[27]. In the Murry Lab, collagen constructs are routinely cast at a cell density of 1.6×10^6 cardiomyocytes and 1.6×10^5 HS-27a stromal cells per 100 μL of construct volume. The Eschenhagen group has previously optimized the cell concentration of their fibrin EHTs at 4×10^5 cardiomyocytes per construct[46]. In order to compare the effect of ECM alone in promoting maturation of hESC-EHTs, my investigation also studies the contractility of constructs seeded in either collagen or fibrin at different cell densities.

Ascorbic Acid Treatment

Ascorbic acid is a key component in collagen synthesis, where it serves as a cofactor for the enzymes prolyl and lysyl hydroxylase. The enzyme prolyl hydroxylase converts proline residues on the procollagen peptide chain to hydroxyproline by using ascorbate acid, O_2, Fe^{2+}, and 2-oxoglutarate as cofactors. Ascorbate is involved with reducing Fe^{3+} formed during the reaction to Fe^{2+}, and becomes dehydroascorbate after the reaction. Fe^{2+} and O_2 form a reactive iron-oxygen complex that along with 2-oxogluterate, hydrolyzes proline residues to form hydroxyproline, and forms succinate and CO_2 as byproducts. Ascorbate is also involved with lysyl hydroxylase. This enzyme requires α-ketogluterate, ascorbate, and oxygen, and converts lysine residues on collagen to hydroxylysine. Succinate and CO_2 are formed as byproducts. Hydroxylysine is necessary for forming intermolecular crosslinks in the helix, and for forming glycosidic bonds for regulating crosslink formation. The lack of ascorbate, characteristic in patients with scurvy, prevents the two hydroxylase reactions from happening, resulting in slow secretion of a collagen protein that is not well cross-linked or tightly wound into a helix[66]. In hESC-EHTs, ascorbic acid treatment at 30 μM has also been shown to promote collagen deposition[41], as well as improve sarcomere

organization, cell-cell contact, alignment, and the active force production of hESC-EHTs in a collagen type 1/Matrigel ECM[40]. As such, my investigation also looks at the effect of ascorbic acid treatment on the contractile dynamics of collagen and fibrin hESC-derived constructs.

Previous Work: Undergraduate Capstone Investigation

My undergraduate bioengineering capstone investigation focused on developing a system to implement afterload on hESC-EHTs by anchoring constructs onto two posts: a ferrous post comprised of PDMS and Fe_2O_3 nanoparticles, and a stiff stainless post to act as a rigid support (Fig. 1-A). The ferrous post deflects under an external magnetic field supplied by a bar magnet, providing the resistive load against which the tissue contracts.

Theory

The visible deflection of the ferrous post is a combination of two forces: the uniformly distributed resistive load (ω) imposed by the magnetic field on the Fe_2O_3 nanoparticles, and the tissue force (P) in the other direction imposed by the beating tissue (Fig. 1-B). The ferrous post can be modelled as a cantilever beam, with a moment of inertia as follows, where r is the post's cross-sectional radius:

$$I = \frac{\pi r^4}{4} \tag{1}$$

When acting alone, the uniformly distributed load (ω) creates a deflection (δ_{Af}) that can then be modelled as follows, where (E) is the Young's modulus of the ferrous PDMS post and (l) is the length of the post (the negative sign is indicative that deflection is occurring towards the left):

$$\delta_{Af} = -\frac{\omega l^4}{8EI} \tag{2}$$

The tissue is located at the top of the post, and the force that it exerts on the ferrous post can be modeled as a point force (T) that creates a deflection (δ_T) (a deflection that is occurring towards the right):

$$\delta_T = \frac{Pl^3}{3EI} \tag{3}$$

Using the law of superposition, it is then possible to sum the two deflections (δ_{Af}) and (δ_T) to give an equation for the net deflection (δ_{net}):

$$\delta_{NET} = \frac{Pl^3}{3EI} - \frac{\omega l^4}{8EI} \tag{4}$$

If the dimensions of the post, the Young's modulus (E), and the uniformly distributed magnetic load (ω) are known, equation 4 can then be rearranged to calculate the amount of tissue force (P) as a function of net deflection (δ_{NET}):

$$P = \left(\delta_{NET} + \frac{\omega l^4}{8EI}\right)\left(\frac{3EI}{l^3}\right) \tag{5}$$

Capstone Investigation: Results

The amount of uniformly distributed load vs. magnet distance was computed by recording the deflection of the ferrous post at various magnet positions, using Eq. 2 to calculate ω (post radius = 0.25mm, length = 5mm, and Young's modulus of PDMS = 2 MPa taken from literature for a 10:1 ratio of base to linker[67,68]), and multiplying by post length l to get force. As expected, uniformly distributed load decayed with magnet distance ($y=0.358e^{-1.043x}$, $R^2=0.9152$) and achieved a peak force of 0.358 mN at a magnet distance of 0 cm (Fig. 1-E).

Afterload studies involved subjecting hESC-derived cardiac tissues to either the magnetic load at a magnet distance of 0 cm, or no magnetic load (controls). Tissues were made with 1×10^6

cardiomyocytes (RUES2, wild type, day 21-36, purity 70-90%) and 2×10^5 HS-27a stromal cells in a collagen scaffold. Constructs were kept under the loading regime for two weeks at which point they were harvested for force measurements. Data on active stress vs. strain indicated that all constructs underwent an increase in active stress with strain, following the Frank-Starling mechanism. There was no significant difference in the slopes or average active stresses between control and afterload tissues (Fig. 1-F). Some of the issues with the first generation of the afterload device were 1) tissue remodeling at the support bar site (Fig. 2-A) and, 2) an inherent preload as the ferrous post bends under the magnetic field, thereby stretching the tissue (Fig. 2-B).

Scope of Thesis

Since completing my undergraduate capstone thesis, my investigation has focused on improving the design of the afterload device, studying afterload development in the growing fetus and optimizing the device to implement a physiologically relevant level of afterload, and testing the time and load dependence of afterload in promoting the maturation of human stem cell-derived cardiac constructs. I also look at how ascorbic acid treatment and ECM type (collagen vs. fibrin) impact the contractility of hESC-EHTs.

Results

Resolving Problems with the Capstone Afterload Device

The two major issues with the first afterload device were 1) tissue remodeling at the support bar site, and 2) the inherent preload caused when the ferrous post bends under the magnetic field. To resolve these issues, three major changes were made to the afterload device.

First, an anti-preload bar was installed to prevent the ferrous post from bending under the magnetic field. Second, the cap was modified to not only prevent the tissue from floating out of the post, but to lock-in the tissue at the top of the ferrous post. Third, the support bar was moved to be in proximity to the rigid post. The lock-in feature of the cap allowed the support bar to be repositioned towards the rigid post, and as such, the entire middle region of the tissue was free from contact with the support bar to void remodeling (Fig. 2-C,D).

Afterload Creep

With these changes in place, we conducted a study to investigate the impact of afterload creep on maturation. Constructs were cast in a collagen type I gel (1.25 mg/mL) at a concentration of 5×10^5 cardiomyocytes (purity: 86.5%, age: day 29) and 5×10^4 HS-27a stromal cells per 30 µL of cell and collagen gel mixture. Four days after casting, no stress constructs were cut from one post, and afterload treatment began (day 4: 0.1 kPa, day 5: 0.3 kPa, day 6: 0.8 kPa, day 7: 1.9 kPa, Table 1). All constructs were harvested at day eight for force measurements. Contractility data from the afterload creep, static stress, and no stress (unloaded) conditions revealed a positive relationship between active stress and strain, indicating the presence of the Frank-Starling effect. However, there were no significant differences in the slope of active stress vs. strain or the average active stress between the three treatment groups. Similarly, there were no differences in the passive stress properties among the three conditions (Fig. 3).

Establishing a Physiological Relevance

To help diagnose why we were not seeing a positive effect of afterload on the contractility of constructs, we wanted to understand the physiological relevance of the amount of

uniformly distributed load (ω) being applied onto the tissues by finding the equivalent left ventricular end systolic blood pressure (LVES-BP).

We first found the corresponding circumferential wall tension (σ_θ) by taking the product of ω and post length ($l = 0.5$mm) to get units of force, followed by dividing by the average cross-sectional area of constructs, 0.5 mm^2. In cardiac physiology, it is generally accepted to use the Law of Laplace (Eqn. 6) to relate tension (σ_θ), pressure(P), radius (r), and thickness (t) for a cylinder, which we can use to model the shape of the ventricle chamber.

$$\sigma_\theta = P * \frac{r}{t} \tag{6}$$

However, the Law of Laplace equation does not apply for thick-walled vessels where the ratio of radius to thickness is less than ten. During fetal development, the LVES inner radius (r_i) ranges from 0.10 ± 0.05 cm at 10 weeks to 0.55 ± 0.05 cm at 40 weeks. This increase in r_i can be modeled by the equation y = 0.015x – 0.05 (y = r_i in cm, and x = gestational age in weeks), which is accurate from ten weeks to term[69]. The LVES wall thickness (t) ranges from 0.14 ± 0.05 cm at 10 weeks to 0.50 ± 0.05 cm at 40 weeks, and can be modeled by the equation y = 0.012x + 0.02 (y = t in cm, and x = gestational age in weeks), which is also accurate from 10 weeks to term[69]. The ratio of radius to thickness is always less than ten during the gestational period, indicating that the Law of Laplace is not ideal for calculating internal pressure.

Lamé's equation (Eqn. 7) accounts for the thickness of the chamber, and incorporates inner radius (r_i) and outer radius (r_o), in addition to internal pressure (P_i) and outer pressure (P_o):

$$\sigma_\theta = \frac{{r_i}^2 P_i - {r_o}^2 P_o}{({r_o}^2 - {r_i}^2)} + \frac{(P_i - P_o){r_i}^2 {r_o}^2}{({r_o}^2 - {r_i}^2) r^2} \tag{7}$$

The outer radius, r_o, is found via the equation $r_o = r_i + t$ and the radius at the midwall, r, is found via the equation $r = r_i + \frac{t}{2}$. We can assume that P_o is negligible, reducing Eqn. 7 to:

$$\sigma_\theta = \frac{{r_i}^2 P_i}{({r_o}^2 - {r_i}^2)}\left[1 + \frac{{r_o}^2}{r^2}\right] \quad (8)$$

Eqn. 8 can be rearranged to solve for LVES internal pressure, P_i:

$$P_i = \frac{\sigma_\theta({r_o}^2 - {r_i}^2)}{{r_i}^2\left[1 + \frac{{r_o}^2}{r^2}\right]} \quad (9)$$

We can assume a LVES internal chamber radius, (r_i) of 0.25 cm and a maximum LVES wall thickness (t) of 0.3 cm corresponding to the dimensions of the LV chamber around 20 weeks for translating ω into LVES-BP[69].

Using Eqn. 9, the corresponding LVES-BP for various ω are found in Table 1. As the magnet in the afterload device is brought closer to the culture dish from 3 cm to 0 cm, LVES-BP increases from 0.2 mmHg to 8.2 mmHg. In the developing fetus, systolic blood pressure ranges from 28 mmHg at 10 weeks to 60 mmHg at 40 weeks (Table 2), indicating that the ferrous posts are not capable of producing high enough magnetic loads[70].

Afterload Using PDMS + Neodymium Posts

In order to increase the amount of magnetic load generated in the afterload device, we decided to try out different magnetic materials to install in the PDMS posts. Three different materials were tested against the existing ferrous PDMS post: metal steel beads with a diameter of 0.5 mm (Next Advance, SSB05), metal beads with a diameter of 2.0 mm (Next Advance, SSB14B), and a 1 cubic millimeter neodymium magnet (Amazon, grade N42). Magnetic strength was determined qualitatively by attaching each material onto the end of uniform strips of paper

and observing deflections at various magnet distances. The 1 cubic millimeter neodymium magnet produced the greatest deflection, followed by the ferrous PDMS post, 2.0 mm metal bead, and 0.5 mm metal bead, in that order. This finding prompted us to generate a new post system that contains the neodymium magnet to produce greater afterloads.

Revising the Afterload System

The diameter and length of the posts needed to be expanded to accommodate the neodymium magnet. This promoted us to redesign the posts and the negatives to also streamline the fabrication process and reduce the five-day fabrication time necessary in the ferrous post system. The new design is based off of the Eschenhagen post array system[32,45], where each post has a cap that tissues wrap onto. Changes to the configuration of the posts and the geometry of the rectangular openings at the surface were made to orient the afterload posts in relation to the external magnet and improve the structural integrity of the array (Fig. 4-A). The neodymium magnet is positioned at the tip of the post, an anti-preload bar prevents bending of the afterload post under the magnetic field, and the rigid support keeps the second post stiff (Fig. 4-B). To increase the magnetic load even further, a larger 4 x 1 x 1 inch external bar magnet (K&J Magnetics) was used to supply the external magnetic field to deflect the posts. The negative to produce the post array consists of four segments that come apart for easy removal of the positive (Fig. 5). Each array occupies one row of six wells of a 24-well plate, and the plate sits in a custom built polycarbonate frame, with a track to allow the external bar magnet to be positioned at specific distances from the plate (Fig. 7).

Characterizing the Mechanical Properties of the PDMS-Neodymium Afterload System

Characterization of the new device's mechanical load profiles was carried out using a micromanipulator as previously described[71]. Calibration of the manipulator tip's stiffness was carried out using a force transducer to record force vs. tip deflection, generating a curve with slope 0.2928 µN/ µm (R^2=0.9954, Fig. 8-A). The calibrated micromanipulator was then used to deflect the PDMS post by various amounts. Deflection of the PDMS post was recorded, and force was calculated by taking the product of manipulator tip deflection and tip stiffness. The force vs. post deflection of three PDMS-only posts generated a highly linear profile as expected, with a post stiffness of 0.85 µN/ µm (R^2=0.9853, Fig. 8-B). Using Eqn. 10 and the dimensions of the post (l = 12.5 mm, r = 0.75 mm), we were able to validate that the stiffness (k) equated to a Young's modulus (E) of 2.6 MPa, which is standard for PDMS made with a 10:1 ratio of base to linker[67].

$$k = \frac{3\pi E r^4}{4l^3} \tag{10}$$

The afterload force vs. magnet distance profile followed a decaying exponential curve with increasing magnet distance ($y = 3720e^{-0.303x}$ where y = µN and x = cm, R^2=0.9811, Fig. 8-C). In comparison with the ferrous posts that achieved a maximum force of 0.358 mN (Fig. 1-E) corresponding to an LVES-BP of 8.2 mmHg (Table 1), the PDMS-neodymium posts produced an over 10-fold greater maximum force of 3.7 mN, corresponding to a LVES-BP of 138.9 mmHg using Lame's equation (Table 2). Using the Law of Superposition, it was possible to combine the PDMS post deflection curve and afterload curve (centered at a magnet distance of 8 cm) to generate the force profile of the afterload post on the tissues as the tissue contracts and bends the post (Fig. 8-D). The combined curve begins at 0 µF when deflection is 0 µm, jumps to 329 µN as

the tissue begins to contract, and then primarily follows the linear increase set by the PDMS force as the magnetic force remains relatively constant.

Time Dependence Afterload Study

Using the new afterload system with PDMS-neodymium posts, we performed a study to see how increasing afterload at a fast rate on constructs from 0 kPa to 8.2 kPa at 1.2 kPa per day for 7 days would impact contractility in comparison to static stress and no stress controls. Constructs were seeded in fibrin gels at a concentration of 4×10^5 cardiomyocytes (purity: 89.6% cTnT positive; age: day 28) and 4×10^4 HS-27a stromal cells per tissue. No stress controls were cut from one post 4 days after casting when afterload treatment began. All tissues were harvested 7 days later for force measurements. Contractility data study testing the faster rate of afterload revealed that constructs undergoing afterload conditioning, static stress, and no stress generated higher active stresses with increases in strain, following the Frank-Starling mechanism (Fig. 9-A). There were no significant differences in the slope of active stress vs. strain among the conditions, however the average active stress for afterload and static stress (1.03 ± 0.23 mN/mm^2) was 9.5-fold higher compared to tissues undergoing no stress (0.11 ± 0.06 mN/mm^2, $p<0.05$). The difference in baseline active stress (at 0% strain) can be attributed to the error in attaching constructs to the transducer at slack length. There was a trend of increasing slope of passive stress vs. strain from no stress to static stress, however the differences were not significant (Fig. 9-B). Taken together, static stress and afterload promoted a 6.7-fold increase in contractile velocity (6.26 ± 1.29 $mN/s{\cdot}mm^2$) compared to no stress (0.94 ± 0.55 $mN/ s{\cdot}mm^2$, $p<0.01$, Fig. 9-C). There was so significant difference among the three groups for the average time to relax to 90% of each contraction (Fig. 9-D).

We simultaneously performed a study to ramp afterload from 0 to 8.2 kPa at a rate of 0.6 kPa/day for 14 days on fibrin constructs made with the same cardiomyocyte and stromal cell population and concentration as the fast afterload study. No stress controls were cut from one post 4 days after casting when afterload treatment began. All tissues were harvested 14 days later for force measurements. All constructs that were a part of the slower afterload study also displayed the Frank-Starling mechanism with higher active stresses as strain was increased (Fig. 10-A). The slope of active stress vs. strain for tissues in the afterload group (0.075 ± 0.001 mN/mm^2) was 12.5-fold higher than no stress (0.006 ± 0.004 mN/mm^2, $p<0.05$). The maximum active stress (at 25% strain) for afterload tissues (3.63 ± 0.12 mN/mm^2) was 18.9-fold higher than no stress (0.21 ± 0.15 mN/mm^2, $p<0.001$). In addition, the maximum active stress for static stress (3.81 ± 0.53 mN/mm^2) was 21-fold higher than no stress ($p<0.001$). There were no significant differences in the slope or maximum active stress between afterload and static stress tissues. The three groups also had no significant differences in their passive stress profiles (Fig. 10-B). Contractile velocity of afterload (20.6 ± 0.6 $mN/s \cdot mm^2$) and static stress (20.6 ± 0.9 $mN/s \cdot mm^2$) were 24-fold greater than no stress (0.8 ± 0.7 $mN/s \cdot mm^2$, $p<0.01$), but there were no significant differences in contractile velocity between static stress and afterload (Fig. 10-C). As with passive stress, there were no significant differences among the three groups for the average time to relax to 90% of each contraction (Fig. 10-D).

Load Dependence Afterload Study

Next, we performed a study testing the effect of holding afterload constant at either 2 kPa or 4 kPa on constructs vs. static and no stress controls. Constructs were seeded at a concentration of 4×10^5 cardiomyocytes (purity: 83.4% cTnT positive; age: day 28) and 4×10^4 HS-27a stromal

cells per tissue in a fibrin gel. No stress controls were cut from one post 4 days after casting when afterload treatment began. All tissues were harvested 14 days later for force measurements. Constructs in the load dependent study holding afterload at 2 kPa all displayed increasing active forces with strain (Fig. 11-A), except for the no stress tissues, which had reduced in length from 4.5 ± 0.25 mm prior to cutting to 1.5 ± 0.15 mm (data not shown) at the end of the experiment duration and were thus not measurable in the force transducer system. Between afterload and static stress conditions, there were no significant differences in active stress, passive stress, contractile velocity, and relaxation time to 90% of contraction (Fig. 11-B,C,D). Similar results were found in the load dependent study holding afterload at 4 kPa, where no stress tissues were unmeasurable in the force transducer system and no significant differences in contractile dynamics occurred between afterload and static stress constructs (Fig. 12). The higher degree of shortening of no stress tissues in this study can be attributed to the proliferation of HS-27a stromal cells allowing further remodeling of the collagen ECM.

Ascorbic Acid Study

Using the new post system, we performed a study that investigated ascorbic acid treatment (30μM in RPMI with B27 supplemented with insulin and aminocaproic acid) as a means to promote contractility of fibrin constructs (4×10^5 cardiomyocytes and 4×10^4 HS-27a stromal cells per construct) and collagen constructs (1.6×10^6 cardiomyocytes and 1.6×10^5 HS-27a) vs. respective non treated controls (constructs were made with the same cell population as the load dependence study). Constructs were treated for 14 days, following which they were harvested for force measurements. The ascorbic acid study on fibrin constructs did not reveal any significant differences in active stress, passive stress, contractile velocity, and relaxation time to

90% of contraction between tissues that were treated with ascorbic acid and those that were not treated (Fig. 13). The same result was found for the ascorbic study on collagen constructs (Fig 14). All constructs that were measured displayed an increasing active force with strain (Fig. 13-A, Fig. 14-A).

Fibrin Collagen Cell Number Study

Using the new post system, we investigated the impact of a collagen vs. fibrin seeded at their respective optimum cell densities on tissue contractility. We cast constructs in either collagen or fibrin gels at either 4×10^5 cardiomyocytes + 4×10^4 HS-27a stromal cells per tissue, or a concentration of 1.6×10^6 cardiomyocytes + 1.6×10^5 HS-27a stromal cells per tissue (constructs were made with the same cell population as the load dependence study). Constructs were kept in culture for 16 days, after which they were harvested for force measurements. Active stress vs. strain curves indicated that fibrin constructs seeded with 4×10^5 cardiomyocytes had a higher average active stress (0.16 ± 0.02 mN/mm^2) than collagen constructs seeded with 4×10^5 cardiomyocytes (0.06 ± 0.02 mN/mm^2, $p<0.05$, Fig. 15-A). There was no significant difference in the slope of active stress vs. strain between these two groups, between fibrin and collagen constructs seeded with 1×10^6 cardiomyocytes, or within the two fibrin and two collagen groups either (Fig. 16-A). Passive stress data did not reveal any significant differences among the four groups as well (Fig. 15-B, Fig. 16-B). Fibrin constructs seeded with 4×10^5 cardiomyocytes had a 2.7-fold greater contractile velocity (0.57 ± 0.03 mN/s·mm^2) than collagen constructs seeded at the same density (0.21 ± 0.04 mN/s·mm^2, $p<0.05$, Fig. 15-C). There was no difference in contractile velocity between fibrin and collagen constructs seeded at 4×10^5 cardiomyocytes (Fig. 16-C). In addition, there were no significant differences in relaxation time to 90% of contraction

among the four groups (Fig. 15-D, Fig. 16-D). Immunofluorescence staining for alpha-actinin and connexin-43 showed aligned and elongated cardiomyocytes, particular in fibrin constructs (Fig. 17), however quantitative analysis will be necessary to confirm these observations.

Discussion

The changes made to the first design of ferrous afterload device built for my capstone project allowed us to eliminate preload effects in our investigation and retain tissue integrity through the experimental period. The anti-preload bar eliminated the interference of stretching as the ferrous post bent under the magnetic field. Since we have already seen that static stretch promotes the contractility of hESC-EHTs[26,51,43,40], incorporating the anti-preload bar allowed us to look at only afterload as a possible mechanism to improve tissue maturation. In our model, the force generated by the tissues on the ferrous post is a point force located at the top of the post. Redesigning the caps on the ferrous posts allowed us to neatly anchor the tissues at the top of the post. This ensured that they would not drift down, which was observed in the first design. Anchoring the tissues onto the cap also allowed us to move the support bar from the center of the construct to the opposite end, near the rigid post. This avoided remodeling at the center of the construct, which would have interfered with the propagation of each contraction.

The study on afterload creep that followed the incorporation of these changes to the device did not reveal any significant difference in contractility (both active and passive stress) between constructs undergoing afterload creep, static stress, or non-stress controls. This promoted us to study how the amount of magnetic load generated by the attractive force between the ferrous post and magnet compared to physiological afterload by converting ω to the equivalent LVES-BP. After translating ω into σ_θ, we used Lamé's equation (Eqn. 7) to find

LVES-BP (P_i) instead of the Law of Laplace (Eqn. 6) since the ratio of the left ventricular internal radius to wall thickness during end systole in the developing fetus is always less than ten. Using literature values for the LVES chamber dimensions[69,70], and assuming a standard construct cross-sectional area of 0.192 mm^2 (circular cross-section with radius = 0.25 mm), we were able to calculate σ_θ in the developing fetus as a function of gestational age (Table 2). We also found that the maximum equivalent LVES-BP in the ferrous afterload system was only 8.2 mmHg when the magnet was adjacent to the tissue culture plate (Table 1). This finding was the motivation to find a way to increase the magnetic load produced by the device.

After conducting a quick and simple test on the magnetic strength of metal beads with different radii, a 1 mm^3 neodymium magnet, and the ferrous post itself, it was quickly found that the neodymium magnet had the highest magnetic strength and was the best candidate for increasing the magnetic load in the afterload device. The dimensions of the magnet were too large to fit in the negative used to build the ferrous post, so we designed a four-component negative that brought fabrication time down from five days to overnight, and was compatible with fibrin and collagen tissues. Fibrin constructs were incompatible in the first afterload design since they would stick to the PDMS well at the base of the ferrous posts. In the new design, fibrin constructs were cast in agarose molds to prevent sticking. With a few adaptations to the casting protocol, the new design was also compatible with casting collagen constructs (see Methods for details. The post array also featured the anti-preload bar and a rigid post to isolate mechanical loading to afterload only and avoid preload. The tissues adhered to the caps on the posts, thus avoiding the need for a support bar. Our micromanipulator measurements on the mechanical load profiles of the PDMS-neodymium posts indicated that these posts were able to generate an over 10-fold increase in maximum magnetic force compared to the ferrous posts, and

17-fold increase in corresponding LVES-BP (8.2 mmHg for ferrous posts, 138.9 mmHg for the PDMS-neodymium posts). The stiffness of the micromanipulator tip was too low to obtain deflection measurements of the PDMS posts reinforced with the metal brace that were used in static stress conditioning.

The time dependence afterload studies revealed significant increases in the active stress profiles and contractile velocities for afterload and static stress conditions compared with no stress conditioning in both fast afterload study (1.2 kPa/day) and slow afterload study (0.6 kPa/day). However, there were no significant differences between afterload conditioning and static stress. The load dependence afterload studies that held afterload at either 2 kPa of 4 kPa revealed no significant differences in the active and passive stress profiles between afterload and static stress tissues. In both load dependence studies, the no stress conditions were unmeasurable in the force transducer system since the tissues had contracted down from 4.5 ± 0.25 mm prior to cutting to 1.5 ± 0.15mm.

Overall, our device simulates afterload by providing a tunable resistance to tissue contractions. As tissues contract, the magnetic load is felt along the tissue's long axis. Guterl previously found that dissected rat papillary muscles anchored onto a force transducer and motor induced rapid increases in myocyte diameter and a reduction in the number of sarcomeres in series in isometric conditioning compared to muscles that were given a 15% contractile strain allowance. Increased afterload *in vivo* reduces myocyte shortening and promotes a lower ratio of length to diameter[72]. Isometric conditioning is considered a severe form of increased afterload, which is why a higher length to diameter ratio was found in papillary muscles treated with isometric condition. This study is similar to our afterload studies, where the resistive force is applied onto the muscle's long axis. In our system, increasing afterload by setting a higher

magnetic resistive load is also creating a more isometric condition since tissues have a harder time shortening during the contractions. The similar contractility between afterload and static stress observed in the time and load dependence afterload studies indicates that constructs in afterload conditioning might not have been able to generate enough force to overcome the magnetic load and shorten, thereby experiencing a similar condition as static stress isometric condition. In accordance with the results found by Guterl's study, if we were to reduce the amount of magnetic load to allow constructs to shorten further, we would expect a decrease in myocyte diameter and an increase in myocyte length compared to isometric conditioning.

In the heart, the increase in myocyte length (eccentric hypertrophy) is driven by volume overload (increased preload), and the increase in myocyte cross-sectional area (concentric hypertrophy) is driven by pressure overload (afterload). Volume overload promotes cell lengthening by the addition of sarcomeres in series due to axial strain[73]. In contrast, increasing systolic pressure during pressure overload increases myocyte radial growth (concentric hypertrophy) because of radial tension developed via cross-fiber strain[74]. It has previously been found that principal transverse strains on NRVMs micropatterned on a deformable elastomer surface increase myofibril accumulation[75]. In a follow up study, it was also found that focal adhesion kinases (FAKs) activate to a higher degree during transverse strain than longitudinal strain. Transverse strains deform the FAKs to initiate mechanotransductional signaling to the sarcomeres for thin filament addition in parallel[73]. It has also been found that transverse strain reduces contractile protein turnover and promotes the aggregation of myofibril subunits in parallel on NRVMs plated on an aligned collagen surface[76]. All together, these studies support the hypothesis that radial hypertrophy is driven by cross-fiber strain rather than longitudinal strains. Parallel addition of myofilaments driven by lateral strain increases the active force

production of myocytes compared with addition of sarcomeres in series driven by longitudinal strain[77–81]. The present afterload device applies a stress in the longitudinal direction, but does not apply a transverse strain on constructs to increase the addition of contractile elements in parallel. This could be why we did not see an increase in force production between afterload and static stress tissues.

Ascorbic acid treatment did not reveal any significant differences in contractile dynamics in collagen and fibrin studies. It has previously been reported that ascorbate treatment stimulates collagen synthesis and proliferation of stromal cells, including human foreskin fibroblasts[82] and bone marrow-derived mesenchymal stem cells[83]. In the ascorbic acid study done by Kensah, hESC-EHTs were doped with 15 – 30% human foreskin fibroblasts[40]. In our study, fibrin and collagen hESC-EHTs were doped with 10% HS-27a stromal cells as routinely performed. The effect of ascorbic acid treatment may be more pronounced if the concentration of HS-27a was increased in our constructs to 15 – 30%.

The study comparing fibrin and collagen EHTs loaded at two different cell densities indicated that fibrin constructs seeded with 4×10^5 cardiomyocytes had a higher average active stress and contractile velocity than collagen constructs seeded at the same density. This finding supports the hypothesis that fibrin promotes a higher degree of maturation of hESC-EHTs than collagen hESC-EHTs seeded the same low cell density. There were no significant differences in contractility between fibrin constructs seeded at 4×10^5 cardiomyocytes and fibrin constructs seeded at 1.6×10^6 cardiomyocytes, indicating that it is not necessary to seed fibrin constructs at a higher cell density than 4×10^5 cardiomyocytes per 100 μL of construct volume.

Conclusions and Future Directions

In summary, we were able to engineer a novel system that applies physiological levels of afterload onto hESC-EHTs. Our new mold system brought fabrication time down from five days to overnight, and produced PDMS posts that were compatible with both fibrin and collagen constructs. With this new system, we performed the first studies to investigate the role of afterload conditioning in promoting the maturation of hESC-EHTs.

It is unclear yet whether ascorbic acid plays a role in improving the contractility of our hESC-EHTs. Introducing a higher concentration of stromal cells within our constructs may amplify the effect of ascorbic acid in promoting collagen deposition and strengthening contractility. Our studies also demonstrated that fibrin constructs were able to generate greater active stresses than collagen constructs seeded at a low cell density, and were comparable to fibrin and collagen constructs seeded at higher cell densities. This finding supports fibrin as a better candidate for tissue engineering since fewer cells would be required per construct and active stress would not be compromised. Repeating our fibrin and collagen investigation with multiple biological replicates would give us a better idea on how robust fibrin is as a matrix of choice in maintaining contractility when seeded with low cell concentrations.

Our afterload results indicate that constructs undergoing different afterload regimes (load and rate dependent afterload) are able to maintain similar active forces as those undergoing static stress. It would be interesting to see if contractility reduces when constructs are subject to a lower amount of afterload, or whether there is an optimum level that promotes and even better contractility than isometric and unloaded conditions. In order to generate cardiomyocytes closer in resemblance to their native counterparts in morphology, one method could be to apply longitudinal and transverse strains to promote sarcomere addition in both series and parallel[77–81].

Constructs can first be stretched in the longitudinal direction to promote the addition of sarcomeres in series, and then stretched in the lateral direction to promote sarcomere addition in parallel. Using this approach, it may be possible to promote both concentric and eccentric hypertrophy of cardiomyocytes in constructs, thereby improving active stresses to hopefully match the contractility of the native myocardium.

Methods

Fabrication of Molds with Ferrous Posts

The ferrous posts were part of a larger mold that contained 4 wells (length: 7mm, width: 2mm, depth: 2mm) for casting tissues, and a pair of posts per well (diameter: 0.5mm, length: 5mm, spacing: 5mm) to anchor the tissues. The negative for the mold was made by laser cutting 7.5mm thick acrylic plastic (Metrix: CreateSpace, Capitol Hill, Seattle). Fabrication of the positive commenced by first mixing PDMS elastomer (Dow Corning, Sylgard 184) at a 10:1 mass ratio of base to linker. Fe_2O_3 powder (Sigma) was added at a 5:1 mass ratio of PDMS mixture to powder. The ferrous PDMS mixture was thoroughly mixed for 2 minutes, followed by degassing in a vacuum desiccator for 30 minutes to remove bubbles. The mixture was poured over the negatives and degassed again for 30 minutes to remove bubbles in the post region. The negatives were then baked at 65ºC overnight. The following day, the excess cured PDMS was cut away using a scalpel, leaving only cured ferrous PDMS in the post region. Fresh PDMS at a 10:1 ratio of base to linker was mixed, degassed for 30 minutes, and poured over the negative to form the wells. The negative was baked again at 65ºC overnight to cure the non-ferrous PDMS. The following day, the positives were carefully removed and each positive was placed on the edge of one well of a 6 well plate (Corning). Fresh PDMS at a 10:1 base to linker ratio was

mixed, degassed, and carefully poured into the well and around the positive, forming a base. The positives were baked again at 65ºC overnight to cure the base. The following day, the molds were removed from the 6 well plate, and one ferrous post from each pair of ferrous posts was removed to install a stainless steel rigid post in its place. The rigid post was formed by bending a stainless steel insect pin (Ento-Sphinx, Size 000) into a staple shape by hand and anchoring one arm into the well to support the tissue, and the other arm into the external PDMS base for structural support. Lastly, caps were installed over the ferrous posts by positioning a strip of thin, non-ferrous PDMS (length: 1.5cm, width: 3mm, depth: 1mm) over the posts using insect pins, and bonding the two segments using fresh PDMS mixed at a 1:10 base to linker ratio. The molds were baked 65ºC overnight to cure the bond, and then autoclaved for casting tissues. The finished molds (Fig. 1-C) was placed in a custom-built apparatus (Fig. 1-D) containing a neodymium bar magnet (1.5" length, 1.5" diameter, K&J Magnetics) that slid along a track, allowing for the user to tune the amplitude of the magnetic load by varying the distance between the magnet and the ferrous post.

Fabrication of Molds with PDMS-neodymium Posts

The negative for generating the PDMS post array were CNC machined according to the schematic in Fig. 5 at Limited Productions, Inc. in Bellevue, WA. The four piece negative was made with acrylic and held together with four dowels. Each piece was washed with Dawn dishwashing soap and air dried to improve PDMS release. PDMS was mixed at a 10:1 ratio of base to linker and degassed in a vacuum desiccator for 30 minutes. A 2 mm rat ear puncher was used to cut discs (2 mm diameter, 0.5 mm thick) of PDMS from a sheet of cured PDMS, and each disc was placed in the cap region on the base segment, ultimately forming the caps on the

posts where the tissues attach. The four negative components were assembled tightly using several C-clamps, and a single 1 x 1 x 1 mm magnet was placed in at the bottom of one post for each pair of posts. A metal brace hand-made from stainless steel insect wire was inserted into the post in each pair to form the rigid post. An array of magnets affixed to the exterior of the negative kept the magnets within the posts oriented such that their magnetic field remained parallel to each other. Two 5-inch clear acrylic rods (1/16" diameter, TAP Plastics) were positioned in the negative to provide structural rigidity to the post array. The degassed PDMS mixture was poured into the negative and degassed for 15 minutes. A 2" x 6" polycarbonate segment was placed over the negative to create a smooth top surface on the post array, and the negative was baked overnight at 65ºC. The following day, the C-clamps were removed and the negative was immediately submerged in 70% ethanol for 10 minutes to facilitate the removal of the positive. The side segments were first removed, followed by the base, and finally the middle. The anti-preload bar formed by laser-cutting a 1/32" thick sheet of PETG (TAP Plastics) into a staple form (height: 8 mm, width: 3 mm) and carefully pierced into the PDMS array.

Direct Differentiation of hESC into Cardiomyocytes

Undifferentiated hESCs of the RUES2 cell line from Rockefeller University were routinely passaged with versene (0.5 mM EDTA and 1.1 mM glucose in PBS) and expanded on Matrigel (BD Sciences) coated 10-cm plates with mouse embryonic fibroblast-conditioned medium (CCM) supplemented with 5 ng/mL basic fibroblast growth factor (Stemgent). When setting up differentiation plates, cells were passaged with versene, gently triturated into single cells, counted with Trypan Blue (Invitrogen) and plated onto Matrigel coated T-75 plates at 10×10^6 cells per plate in 30 mL CCM supplemented with 5 ng/mL basic fibroblast growth factor

and 1 µM Chiron 9920 (Cayman) per plate. The next day (defined as day 0), differentiation was initiated by feeding cells with 20 mL of RPMI medium (Invitrogen) with B7 supplement without insulin (Invitrogen), 100 U/mL penicillin G, 100 mg/mL streptomycin, and 100 ng/mL activin A (R&D Systems). The following day (day 1), the medium was carefully removed and 30 mL of the same medium without activin A was supplemented with 5 ng/mL BMP4 (R&D Systems) and 1 µM Chiron 9902 at 30 mL per plate. After 48 hours (day 3), the medium was carefully removed and cells were fed with the same medium supplemented with 1 µM Xav 939 (Tocris Bioscience) at 30 mL per plate. Plates were fed with 30mL of the same medium without Xav 939 on day 3 and 5. On Day 7 and every other day following, cells were fed with 30 mL of RPMI supplemented with B27 containing insulin (Invitrogen). Spontaneous beating began between days 8 – 11. On day 20, cells were heat shocked at 42ºC for one hour. The following day, cells were washed with PBS and trypsinized into single cells. Cells were centrifuged and resuspended in CryoStor CS10 freezing medium (StemCell), and transferred to cryovials at 20×10^6 cells per vial in 500 µL of freezing medium. Vials were cooled to -80ºC at a rate of -1ºC per minute in a controlled rate freezer, kept in a -80ºC freezer overnight, and transferred to liquid nitrogen for future use. One week prior to generating constructs, cells were thawed by gentle agitation in a 37ºC water bath, and 20 mL of RPMI with B27 containing insulin was added dropwise to avoid osmotic shock. Cells were counted with Trypan Blue and plated at 1×10^6 cells per well in 6-well plates with 3 mL of RPMI with B27 containing insulin supplemented with 10 µM ROCK inhibitor Y27632 (Tocris Bioscience). Media was changed every other day for seven days. Spontaneous beating would resume 2-5 days after thawing.

Generation of Collagen Constructs in Ferrous Posts

Prior to casting tissues, pre-autoclaved ferrous posts were loaded into 35-mm tissue culture plates (Corning) and soaked with 5% pluronic acid (w/v in sterile deionized water, Sigma) for at least one hour. During this time, cells were trypsinized into single cells and counted using Trypan Blue. 5×10^5 cells were fixed in 4% paraformaldehyde for 15 minutes and kept in 5% FBS in PBS at 4ºC for later purity analysis via flow cytometry. Each tissue contained 5×10^5 cardiomyocytes, and 5×10^4 HS-27a stromal cells. The two cell populations were counted, combined and mixed with a collagen gel on ice, forming a cell-gel solution. The gel consisted of collagen type 1 (final concentration 1.25 mg/mL, neutralized with NaOH; Invitrogen), 11% v/v mouse basement membrane extract (Geltrex, Invitrogen), and 57% v/v medium (RPMI supplemented with B-27 with insulin). The ferrous posts were washed twice with PBS to remove any leftover pluronic acid, and 30 µL of cell-gel solution was gently poured into each tissue well. The freshly cast tissues were incubated at 37ºC for 30 minutes to harden. RPMI supplemented with B-27 with insulin was gently poured into the well and the tissues were fed with the same media every other day.

Generation of Fibrin Constructs in PDMS-neodymium Posts

Spacers (Fig. 6) were 3-D printed (Metrix: CreateSpace, Capitol Hill, Seattle) and were used to generate the agarose wells for casting tissues. The PDMS-neodymium posts cannot be autoclaved since the 1 mm^3 magnet will lose its magnetism above its 80ºC Curie temperature[84]. Thus, to sterilize the posts, each post and spacer was placed in 70% ethanol for 20 minutes, and washed twice in sterile water for 20 minutes each time. 1.5 mL of 2% agarose (in PBS, Sigma)

was poured into each well of a 24 well plate (Corning), and the spacers were inserted over the wells such that their rectangular extrusions were submerged part way into the agarose. After solidification of the agarose, the spacers were carefully removed, leaving wells to cast the fibrin tissue in. The sterilized posts were positioned such that the tip of each post was centered in the agarose well. Cells were trypsinized into single cells and counted using Trypan Blue. 5×10^5 cells were fixed in 4% paraformaldehyde for 15 minutes and kept in 5% FBS in PBS at 4ºC for later purity analysis via flow cytometry. Each fibrin tissue contained 4×10^5 cardiomyocytes, and 4×10^4 HS-27a stromal cells. The two cell populations were counted, combined and brought to a volume of 89 µL per tissue and kept on ice. 2.5 µL of fibrinogen (200 mg/mL, Sigma) and 5.5 µL of 2x DMEM (Invitrogen) was added to the cell mixture. For each tissue, 3uL of thrombin (100 U/mL, Sigma) was aliquoted into an Eppendorf tube. 97µL of cell solution was added into the Eppendorf tube and quickly pipetted into the agarose well. The freshly cast fibrin tissues were incubated at 37ºC for 80 minutes to harden. The tissues were then transferred out of the agarose wells and into a new 24-well plate where they were fed with RPMI supplemented with B-27 with insulin and 5 mg/mL of aminocaproic acid (Sigma) to prevent fibrin degradation. Tissues were fed with the same media every other day.

Generation of Collagen Constructs in PDMS-neodymium Posts

To avoid collagen from adhering to the agarose wells, wells were formed with PDMS beforehand by adding 1.5mL of PDMS (10:1 mixing ratio) to each well of a 24-well plate and inserting the spacer. The plate was kept at 65ºC overnight to cure the PDMS, and the spacers were removed the next day. The wells, along with the PDMS posts, were sterilized using the same ethanol technique used in generating fibrin tissues. After sterilization, the PDMS wells

were coated with 5% pluronic acid for one hour to prevent the collagen tissues from adhering to the well. To improve the adhesion of collagen to the tips of the posts, the posts were treated with 0.1% polyethylenimine (Sigma) and 0.01% glutaraldehyde (Sigma). The treated posts were positioned into the PDMS wells. Collagen constructs were seeded with either 4×10^5 cardiomyocytes or 1.6×10^6 cardiomyocytes, according to the experimental conditions being tested, along with a 10% HS-27a stromal cells. Cells were combined with the collagen gel as described for the ferrous post system, and the cell-gel mixture was carefully loaded into the PDMS wells at 100 µL per tissue. The collagen constructs were incubated at 37ºC for 80 minutes and were transferred out of the PDMS wells and into a new 24-well plate containing RPMI supplemented with B-27 with insulin. Constructs were fed every other day with the same medium.

Cardiomyocyte Purity Analysis

Fixed cells were incubated with 5% FBS/0.75% saponin (Sigma) in PBS containing a cTnT antibody (mouse IgG1, Thermo Scientific Clone13-11, 1:100 dilution) for 30 minutes at room temperature. Samples were then washed twice with 5% FBS/0.75% saponin in PBS and stained with the secondary antibody (goat anti-mouse-IgG-PE, GαM-PE, 1:200 dilution) for 30 minutes at room temperature in the dark. Each sample was washed 3 times with 5% FBS in PBS and re-fixed in 1.3% PF. Samples were analyzed within 7 days on a BD FACS Canto II machine (BD Biosciences). A mouse IgG1 isotype control antibody (eBioscience, 1:100 dilution), in conjunction with the same secondary, was used to gate samples at 5% error with FlowJo version 9.3.1 software.

Mechanical Measurements

Constructs were either removed from the ferrous posts or cut from the PDMS-neodymium posts and anchored onto a force transducer (Aurora Scientific, model 400A) and a length controller (Aurora Scientific, model 308B). The initial length was determined by measuring the total length of each construct under a dissecting microscope and matching the measurement under the force transducer system by adjusting the position of the force transducer hook. Constructs were perfused in 37ºC Tyrode's buffer (containing, in mmol/L: CaCl2 1.8, MgCl2 1.0, KCl 5.4, NaCl 140, HEPES 10, NaH2PO4 0.33, glucose 5,; pH 7.4). Length was increased to 25% strain in 6 steps, and constructs were paced at 1.5 Hz (8V, 50ms pulse duration). Force, length, and stimulation data was recorded for each tissue and analyzed with a custom Matlab software. 6 to 25 contractions were analyzed for each step. Forces were normalized to cross-sectional area, determined by measuring the width and depth of each tissue and assuming an oval cross-section. Two to three constructs were measured for each experimental condition.

Immunostaining

For immunohistochemistry, constructs were fixed for 15 minutes in 4% paraformaldehyde, cryoprotected in 30% sucrose solution overnight, and frozen into cryoblocks using OCT compound (Tissue-Tek) and a 95% ethanol/dry ice slurry. Cryoblocks were sectioned into 10 µm slices at cutting angle of 4º and left to dry overnight. Sections were then rehydrated in blocking buffer (1.5% normal goat serum and 0.1% Triton-X100 in ICC PBS) for 30 minutes, before being loaded with the primary antibody for overnight incubation at 4ºC. The following day, the sections were washed three times with PBS and incubated with the secondary antibody

for one hour, washed three times in PBS and cover-slipped with Vectashield + DAPI mounting medium (Vector Laboratories) for visualizing nuclei. The following primary antibodies were used: mouse anti-α-actinin (Sigma, 1:800 dilution), and rabbit anti-connexin-43 (Sigma, 1:400 dilution. Immunofluorescent secondaries included Alexa 488- or 594-conjugated goat anti-mouse of donkey anti-rabbit antibodies (Invitrogen, 1:100 dilution).

Statistical Analysis

All error bars represent standard error of the mean (SEM). Significance was determine using a single factor ANOVA following a student's t-test using two tails distribution and two sample unequal variance with a 95% or greater confidence level.

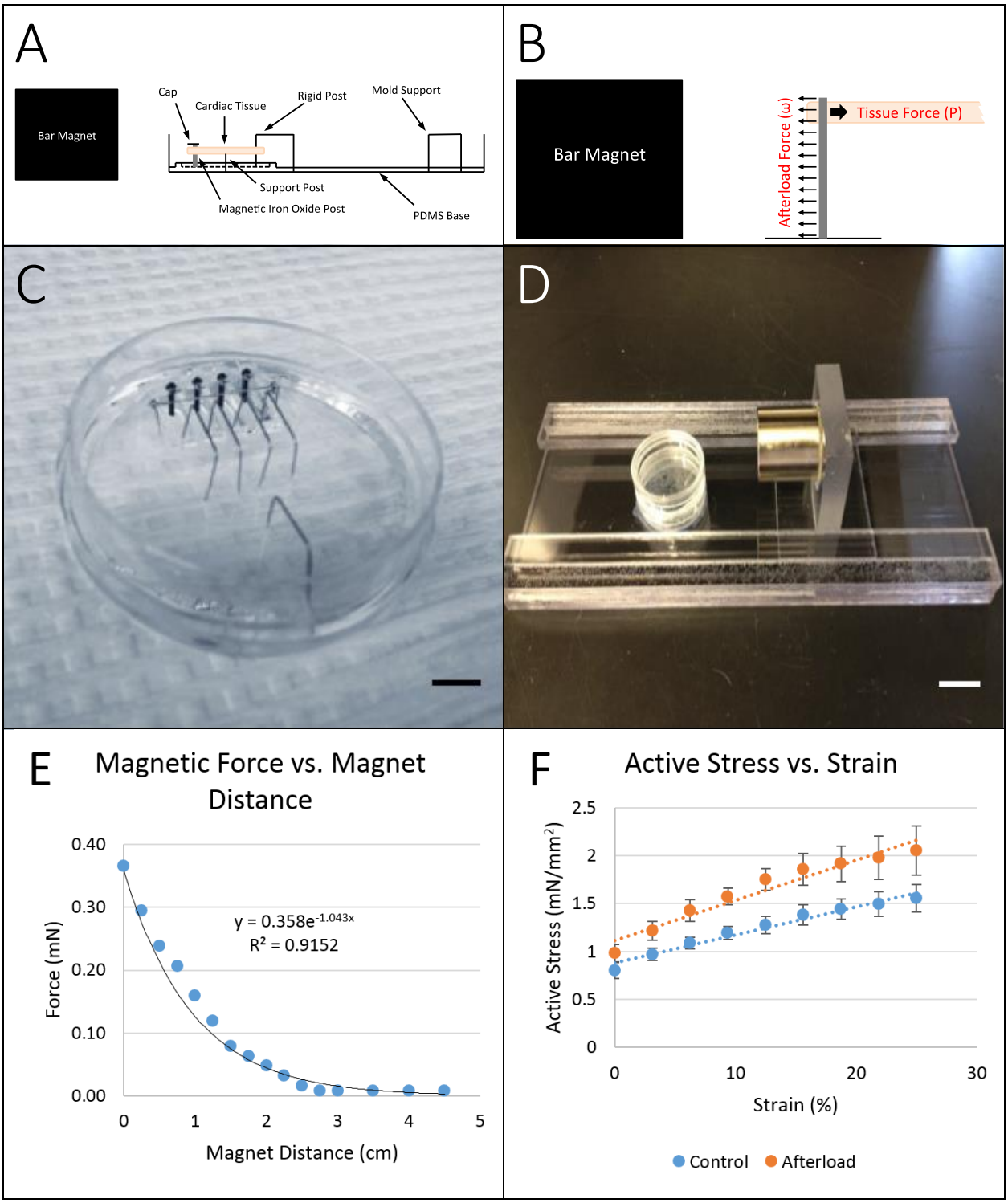

Figure 1: Capstone afterload device diagrams and results. Panel A: Schematic of the afterload system. Panel B: Representation of the uniformly distributed magnetic load (ω) and the tissue force (P). Panel C: Image of the finished afterload culture dish (scale = 5mm). Panel D: Image of the afterload frame (scale = 5mm). Panel E: Force vs. magnet distance profile. Panel F: Sample active stress vs. strain for control tissues ($y=0.0292x+0.8801$, $R^2=0.9699$) and afterload tissues ($y=0.0417x+1.1168$, $R^2=0.9431$). All error bars are ± SEM.

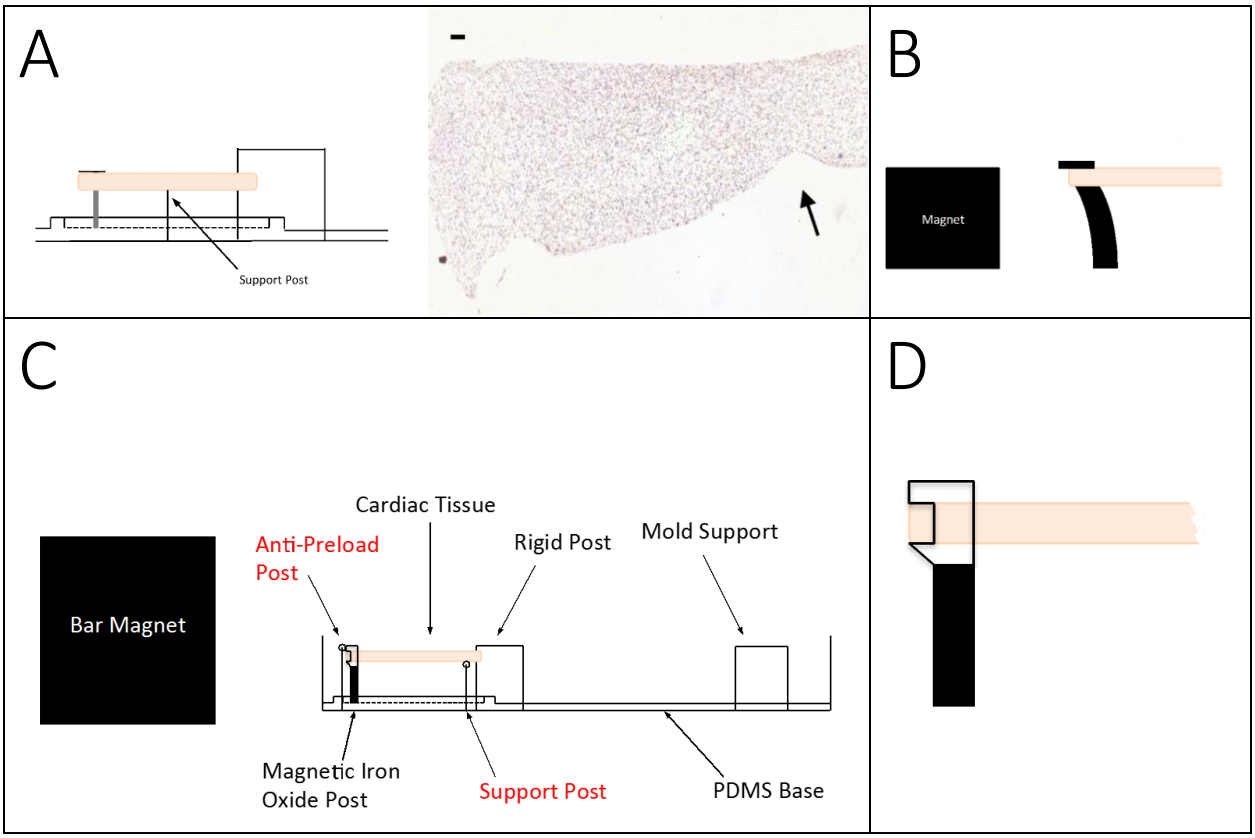

Figure 2: Issues with capstone afterload device and solutions. Panel A: The support post positioned between the afterload post and the rigid post on the capstone afterload device promoted tissue remodeling at the support site, as indicated by the arrow on the hematoxylin and eosin stain (scale = 100µm). Panel B: The tissue stretches as it bends under the magnetic field, creating an inherent level of preload in the device. Panel C: Modifications to the device were made to include an anti-preload post to prevent the ferrous post from bending under the magnetic field, a modified cap to anchor the tissue onto on one end, and the support bar repositioned to be adjacent to the rigid post. Panel D: A larger schematic at the remodeled cap, where tissues are lifted up from the well and lock into the cap region.

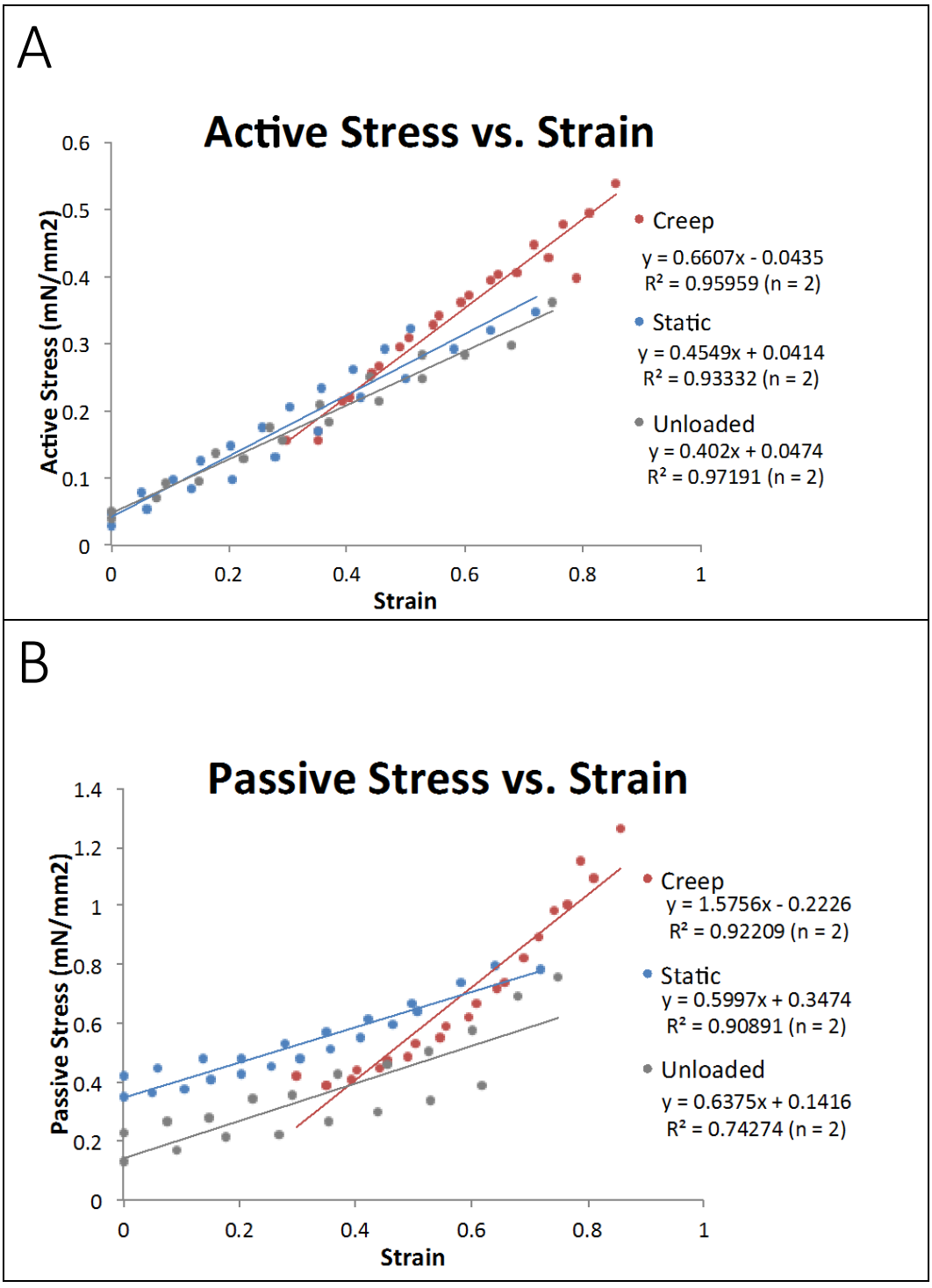

Figure 3: Contractility data from constructs in the improved afterload device. Panel A: Active stress vs. strain for afterload and control tissues. Panel B: Passive stress vs. strain for afterload and control tissues. All error bars are ± SEM.

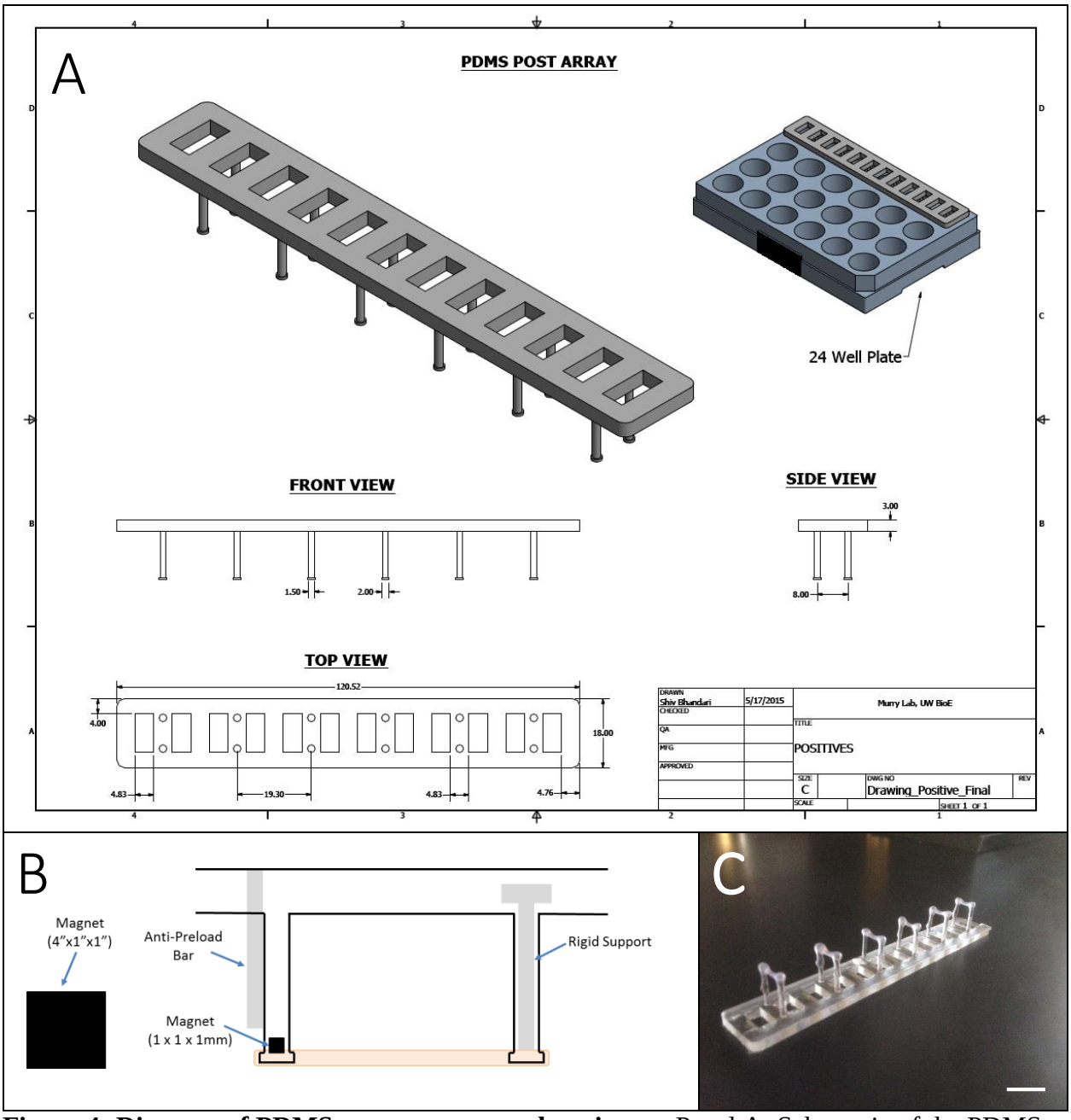

Figure 4: Diagram of PDMS post array to anchor tissues. Panel A: Schematic of the PDMS post array. The PDMS post array holds six tissues—one tissue on each pair of posts, and sits on top of a 24-well plate. The rectangular openings at the top of the array are present for accessibility when casting tissues and removing tissues at the end of each experiment. The ends of each pair of posts contains a cap where tissues anchor onto. Panel B: Schematic of a pair of posts in the array with the afterload post adjacent to an anti-preload bar containing a neodymium 1 x 1 x 1 mm magnet, and rigid post containing a brace or rigid support. The external 4 x 1 x 1" magnet provides the magnetic field for post deflection. Panel C: Image of the post array with tissues anchored to the tip of each set of posts (scale = 1cm).

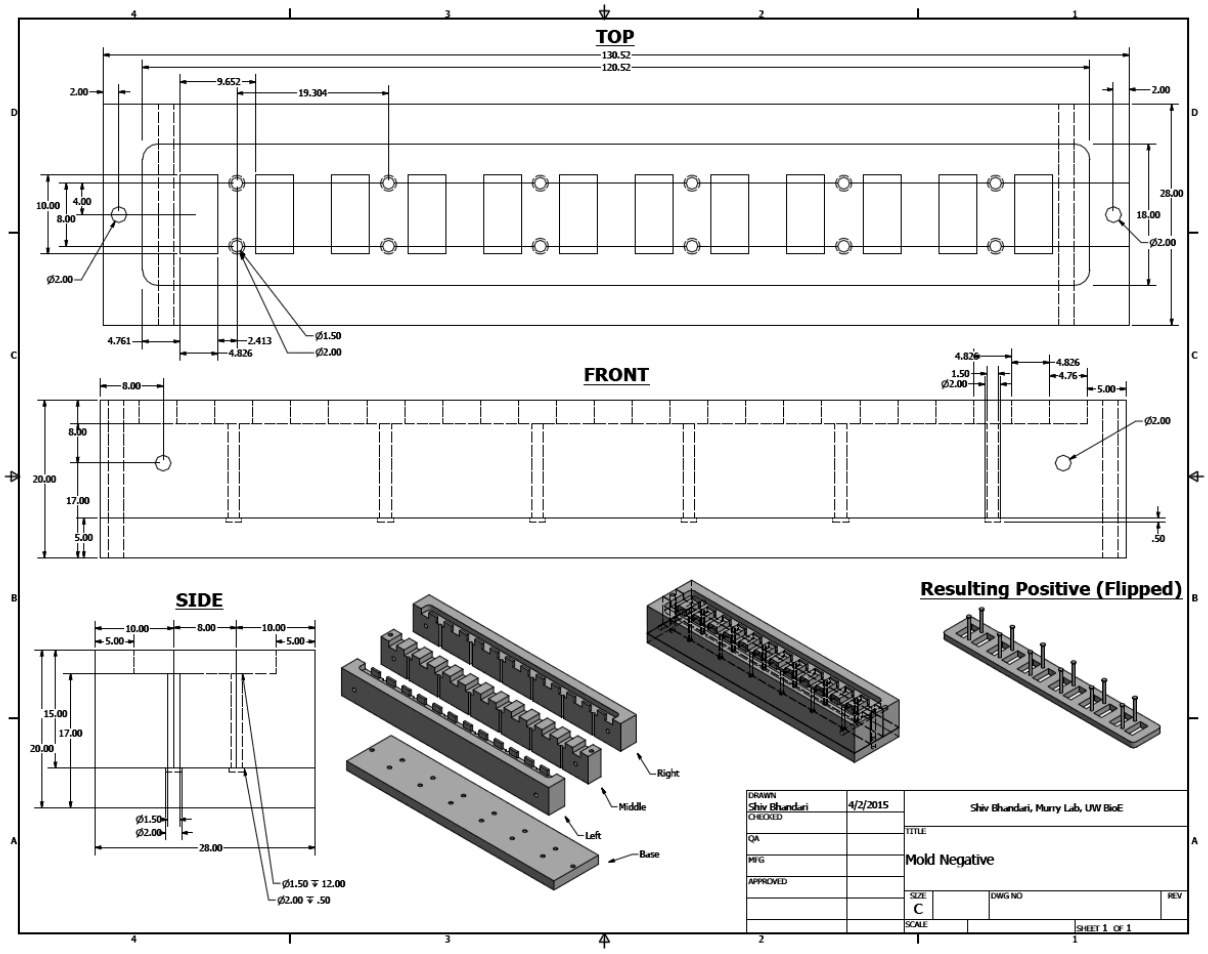

Figure 5: Diagram of negative for PDMS post array. The negative for creating the PDMS post array consists of four components that come apart to remove the finished PDMS array. The four components are CNC-machined from clear acrylic and are held together with four dowels.

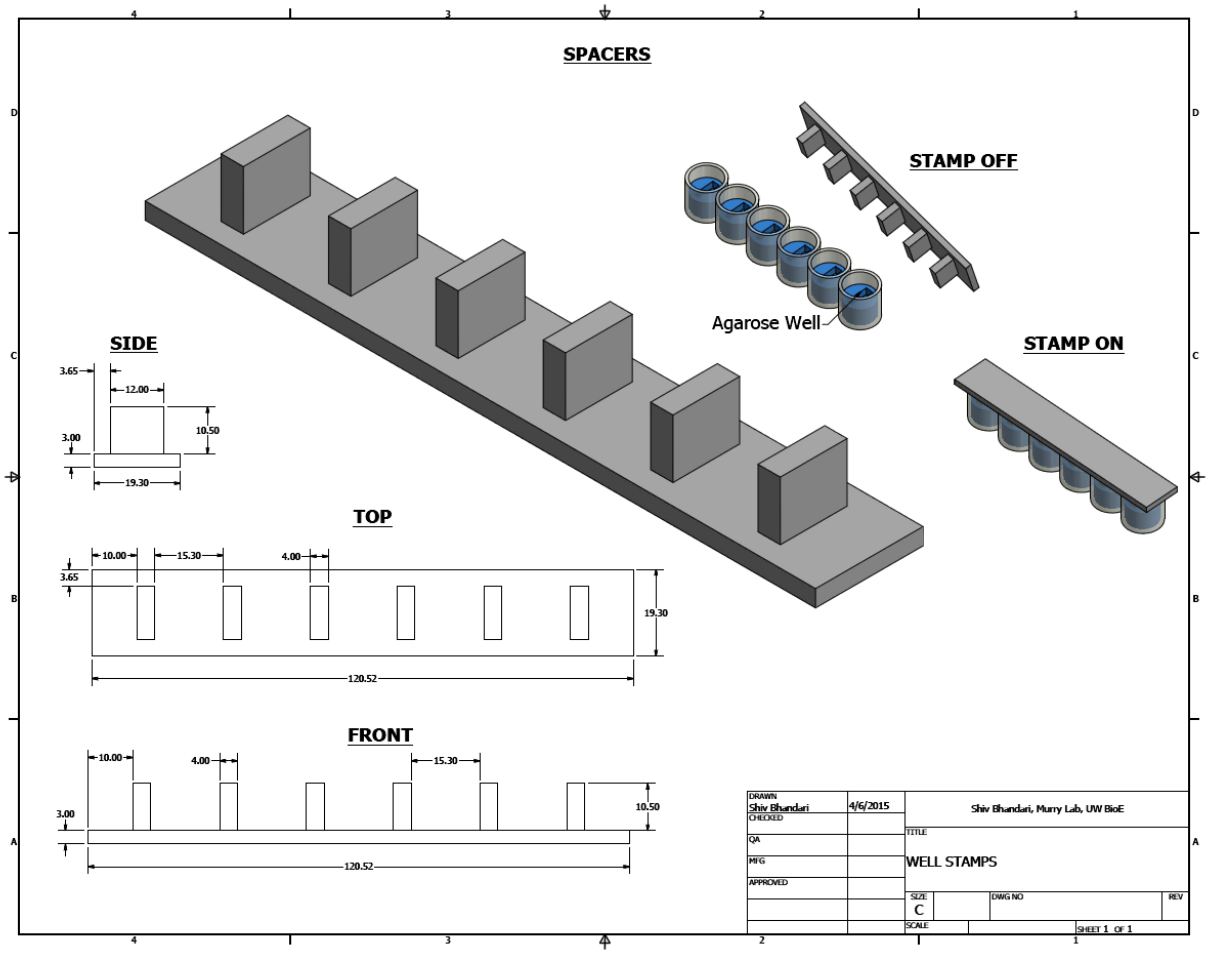

Figure 6: Diagram of spacers to stamp agarose wells for casting tissues. Spacers are 3-D printed and are used to create wells to cast tissues in. After filling wells of a 24-well plate with melted agarose, the spacer is placed over the wells such that the ends of each of the six rectangular extrusions is partially submerged into the agarose. After cooling, the spacer is removed, leaving a hardened agarose well in the shape of the rectangular segment to cast tissues.

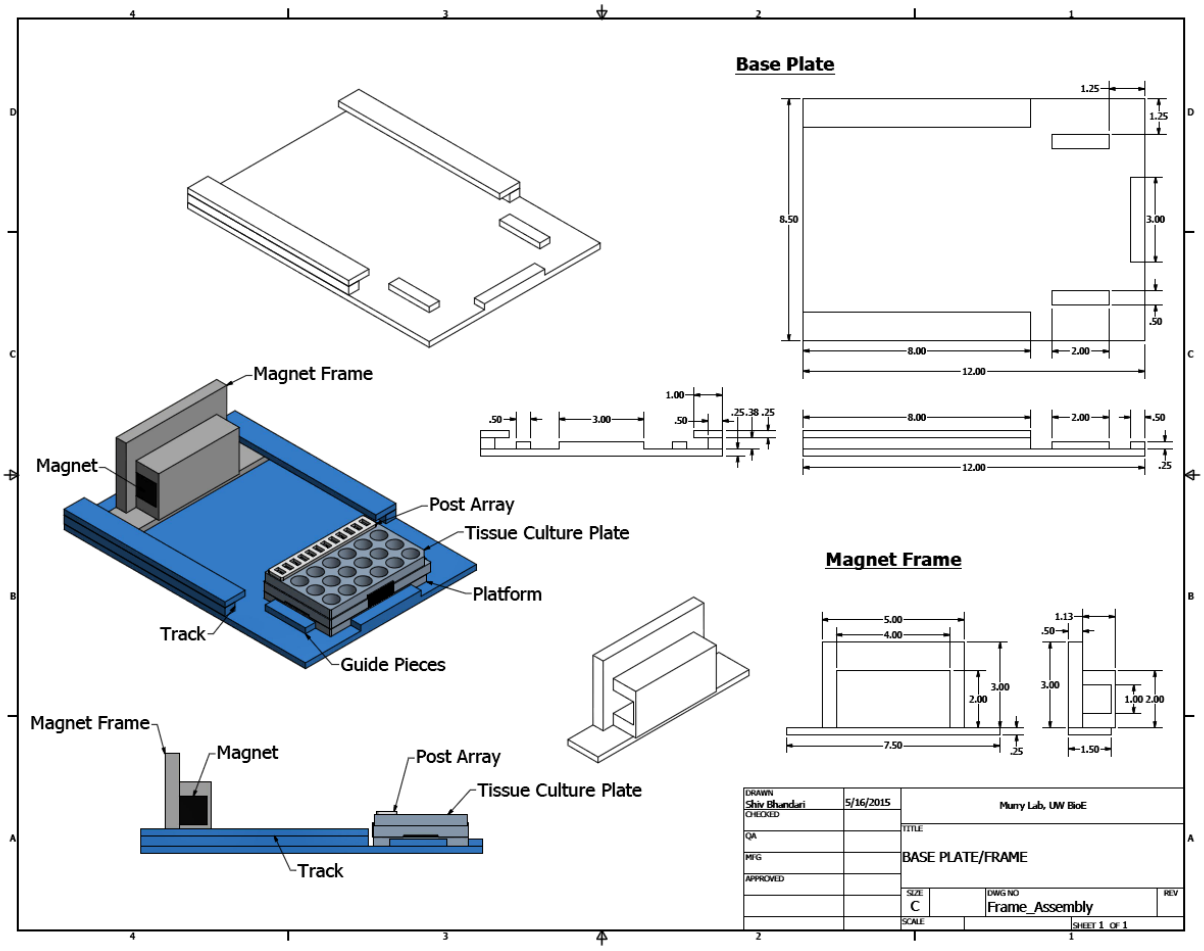

Figure 7: Diagram of frame for afterload device. All components of the afterload frame are custom-built with polycarbonate. The frame of the afterload device consists of a track mounted onto a polycarbonate base to allow a bar magnet that sits in a holder to slide in the direction of the 24-well plate. Three polycarbonate segments are bonded onto the base to keep the tissue culture plate stationary. Bringing the magnet closer to the plate increases the amount of afterload placed on the tissues in the 24-well plate.

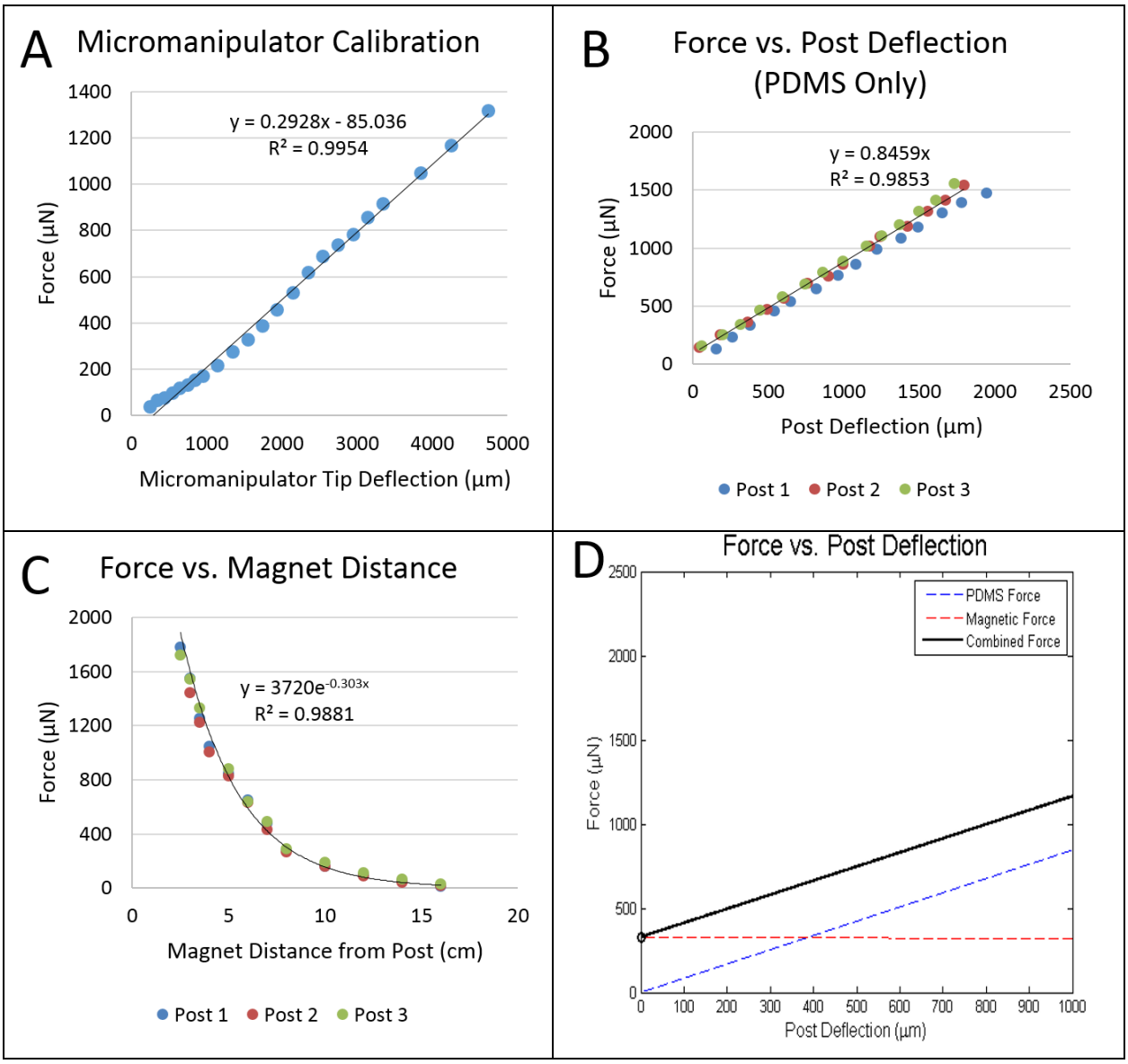

Figure 8: Characterizing the force profiles of the magnetic afterload posts. Panel A: Force profile to obtain the stiffness (0.2928 µN/µm, R^2=0.9954) of the micromanipulator tip used to calibrate all posts. Panel B: Force vs. deflection data for three PDMS posts obtained with the calibrated micromanipulator. Forces follow Hooke's law, $F = k \cdot x$, revealing a post stiffness of 0.8459 µN/µm, R^2=0.9853. Panel C: Data on force vs. magnet distance from the afterload posts using the manipulator, following an exponential decay ($y=3720e^{-0.303x}$, R^2=0.9881) as the magnet is placed further away. Panel D: The two regression curves in panels B and C are summed to give the force profile of the afterload post on the tissue as the tissue contracts and bends the post. The magnetic curve is shifted to model the magnetic force when the magnet is 8 cm away at a post deflection of 0 µm. The combined curve begins at 0 µF when deflection is 0 µm, jumps to 329 µN (open circle) as the tissue begins contracts, and then primarily follows the linear increase set by the PDMS force (blue-dashed curve) as the magnetic force remains relatively constant (red-dashed curve).

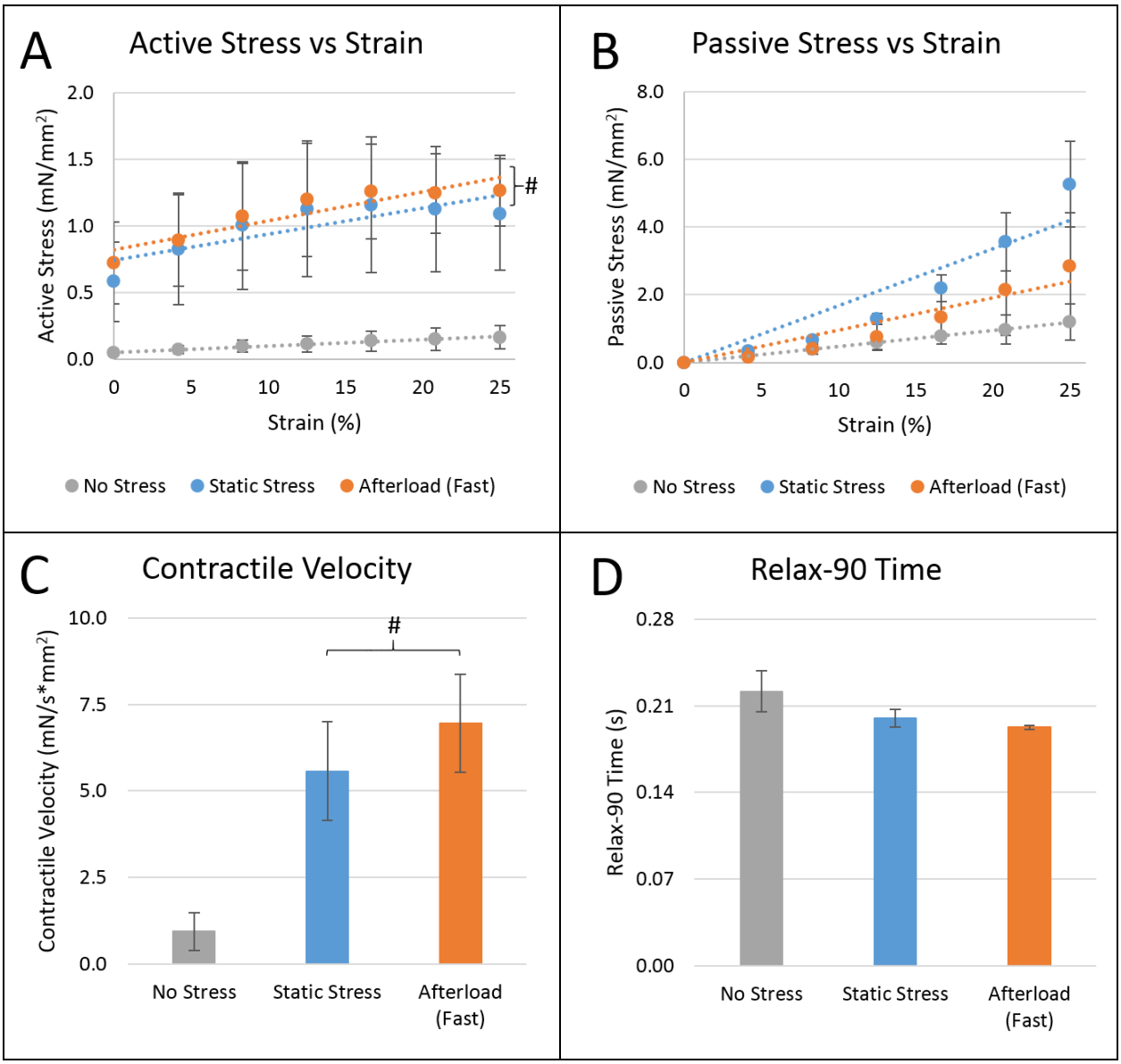

Figure 9: Contractility of fibrin tissues under no stress, static stress, or increasing afterload at 1.2 kPa/day (FAST). Panel A: Active stress vs. strain curves for no stress ($y=0.0047x+0.0505$, $R^2=0.9838$), static stress ($y=0.0195+0.7418$, $R^2=0.6854$), and tissues undergoing afterload conditioning at 1.2 kPa/day for 7 days until an afterload of 8.2 kPa ($y=0.0217x+0.8189$, $R^2=0.8465$). The average active stresses for afterload and static stress combined is 9.5-fold greater than no stress conditioning (#: $p<0.05$). Panel B: Passive stress vs. strain curves for no stress ($y=0.0473x$, $R^2=0.9988$), static stress ($y=0.1682x$, $R^2=0.8714$), and afterload conditioning ($y=0.0960x$, $R^2=0.8960$). Panel C: Contractile velocities for each condition, where the average velocity for afterload and static stress combined is 6.7-fold higher than no stress conditioning (#: $p<0.01$). Panel D: Time to 90% relaxation of contraction for no stress, static stress, and afterload conditioning. All error bars are ± SEM.

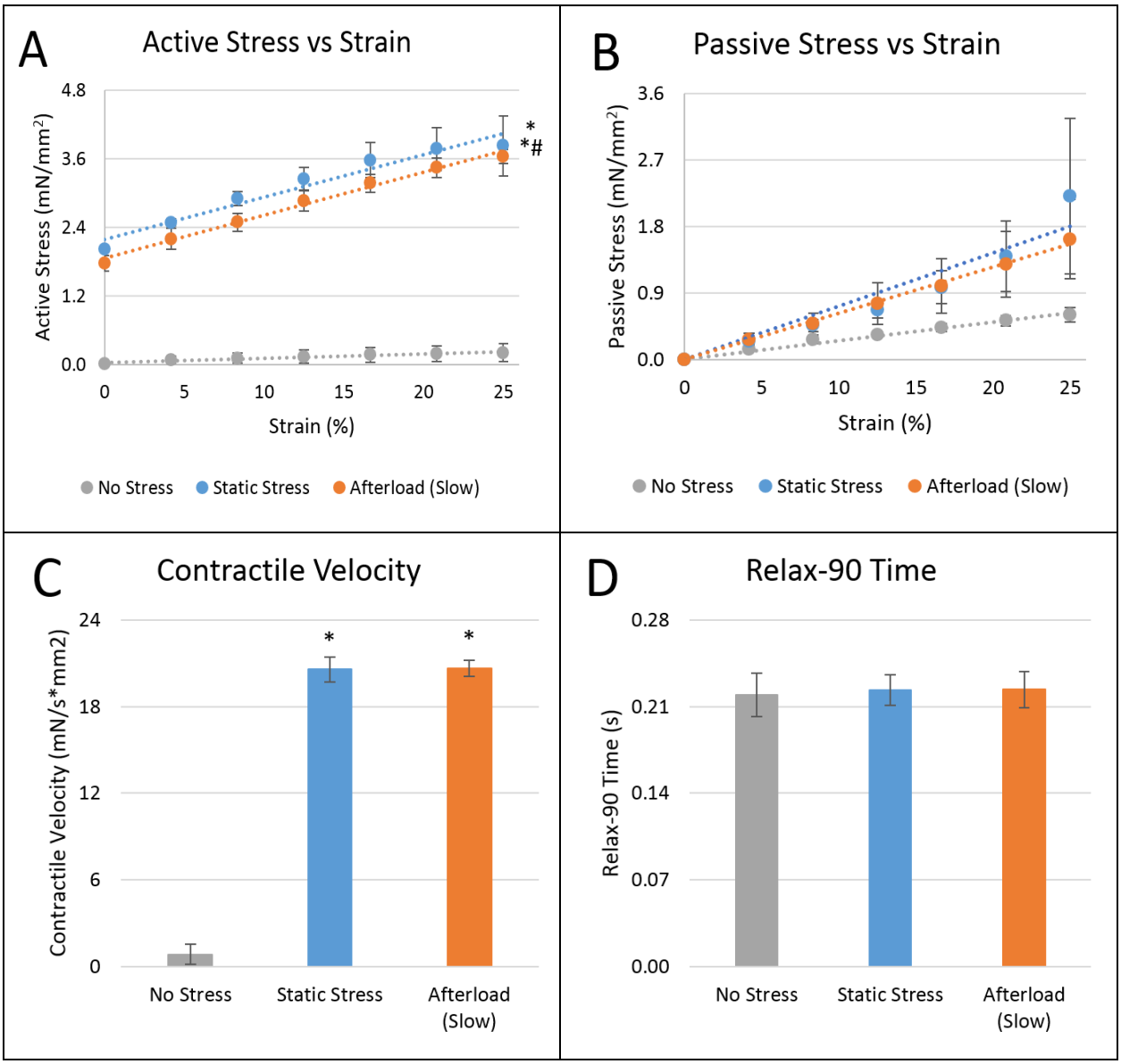

Figure 10: Contractility of fibrin tissues under no stress, static stress, or increasing afterload at 0.6 kPa/day (SLOW). Panel A: Active stress vs. strain curves for no stress ($y=0.0073x+0.0382$, $R^2=0.9444$), static stress ($y=0.0742+2.1872$, $R^2=0.9552$), and tissues undergoing afterload conditioning at 0.6 kPa/day for 14 days until an afterload of 8.2 kPa ($y=0.0752+1.8531$, $R^2=0.9900$). The slope for afterload tissues is 12.5 fold higher than no strain (#: $p<0.05$). The maximum contractility (at 25% strain) for afterload tissues is 18.9 fold greater than no stress, and the maximum contractility for static stress is 21-fold greater than no stress (*: $p<0.001$). Panel B: Passive stress vs. strain curves for no stress ($y=0.0255x$, $R^2=0.9797$), static stress ($y=0.0722x$, $R^2=0.9122$), and afterload conditioning ($y=0.0627x$, $R^2=0.9958$). Panel C: Contractile velocities for each condition, with a 24-fold increase for static stress and afterload tissue compared with no stress (*: $p<0.01$). Panel D: Time to 90% relaxation of contraction for no stress, static stress, and afterload conditioning. All error bars are ± SEM.

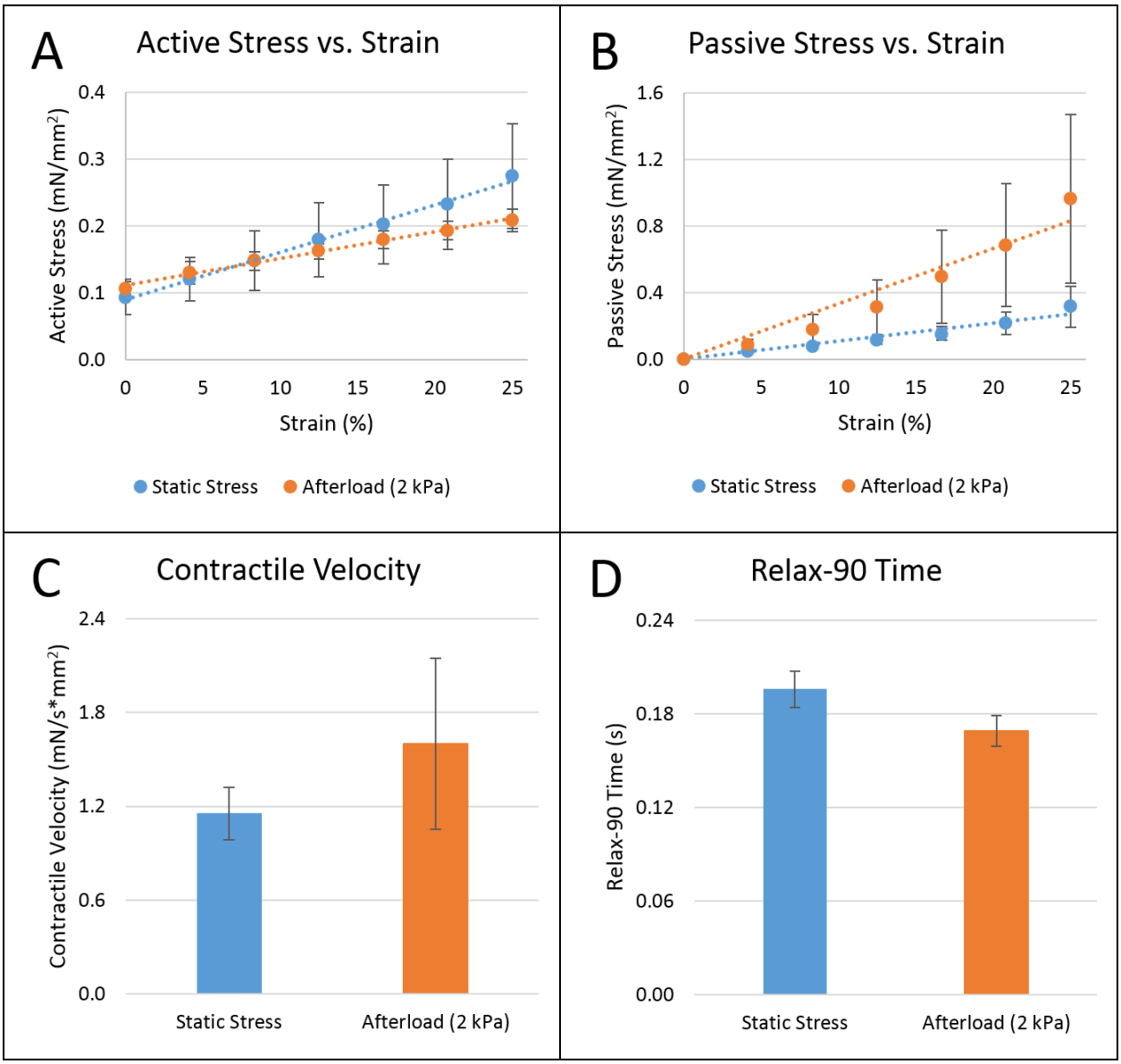

Figure 11: Contractility of fibrin tissues undergoing 2 kPa afterload vs. static stress. Panel A: Active stress vs. strain curves for tissues held at static stress ($y=0.0071+0.0899$, $R^2=0.9949$) and under static afterload conditioning at 2 kPa for 14 days ($y=0.0040x+0.1108$, $R^2=0.9927$). Panel B: Passive stress vs. strain curves for static stress ($y=0.0109x$, $R^2=0.9552$) and afterload ($y=0.0331x$, $R^2=0.9395$). Panel C: Contractile velocity for static stress and afterload conditions. Panel D: Time to 90% relaxation of contraction for no stress, static stress, and afterload conditioning. All error bars are ± SEM.

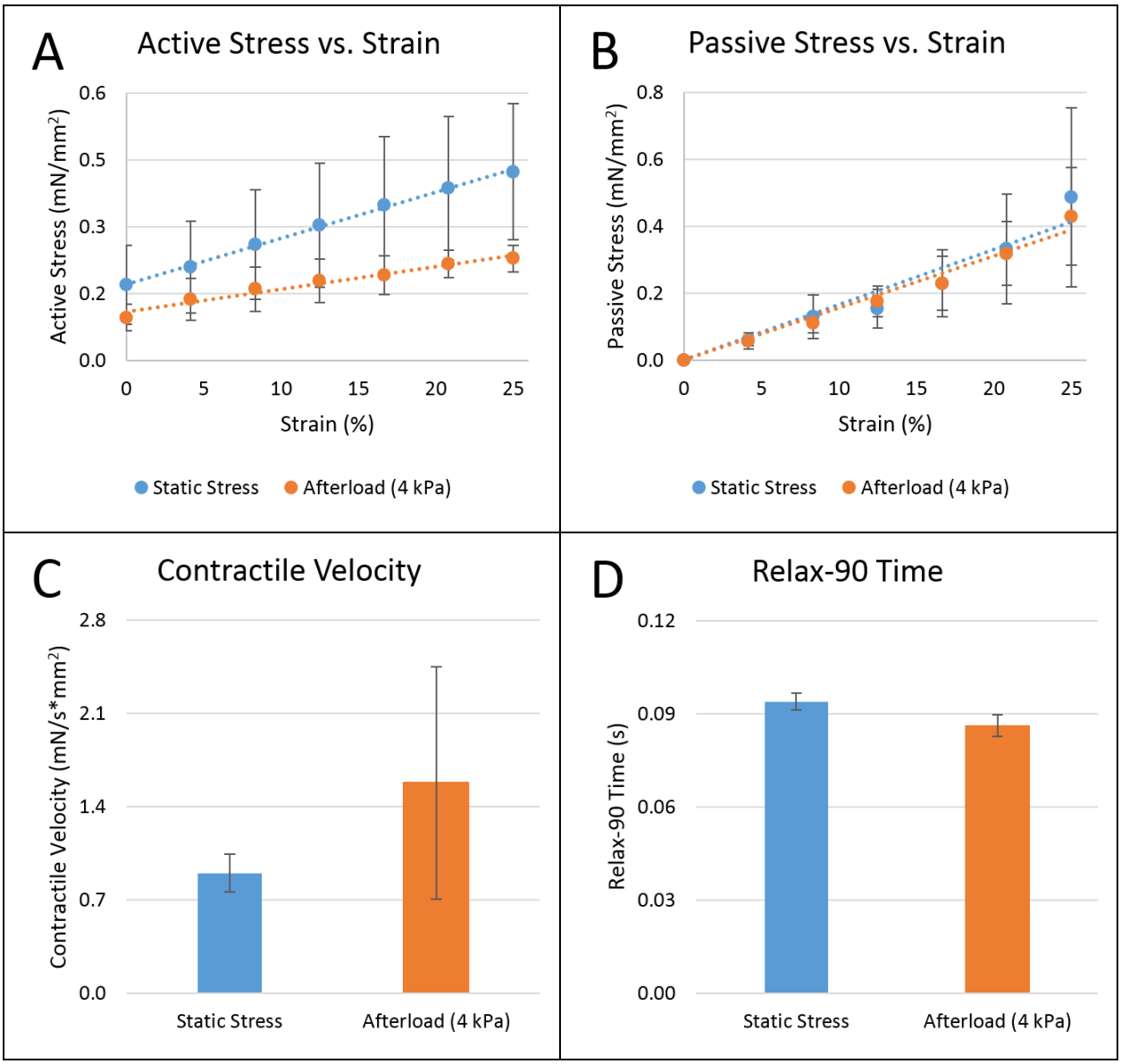

Figure 12: Contractility of fibrin tissues undergoing 4 kPa afterload vs. static stress. Panel A: Active stress vs. strain curves for tissues held at static stress ($y=0.0103+0.1710$, $R^2=0.9976$) and under static afterload conditioning at 4 kPa for 14 days ($y=0.0051x+0.1092$, $R^2=0.9699$). Panel B: Passive stress vs. strain curves for static stress ($y=0.0165x$, $R^2=0.9377$) and afterload ($y=0.0155x$, $R^2=0.9753$). Panel C: Contractile velocity for static stress and afterload conditions. Panel D: Time to 90% relaxation of contraction for no stress, static stress, and afterload conditioning. All error bars are ± SEM.

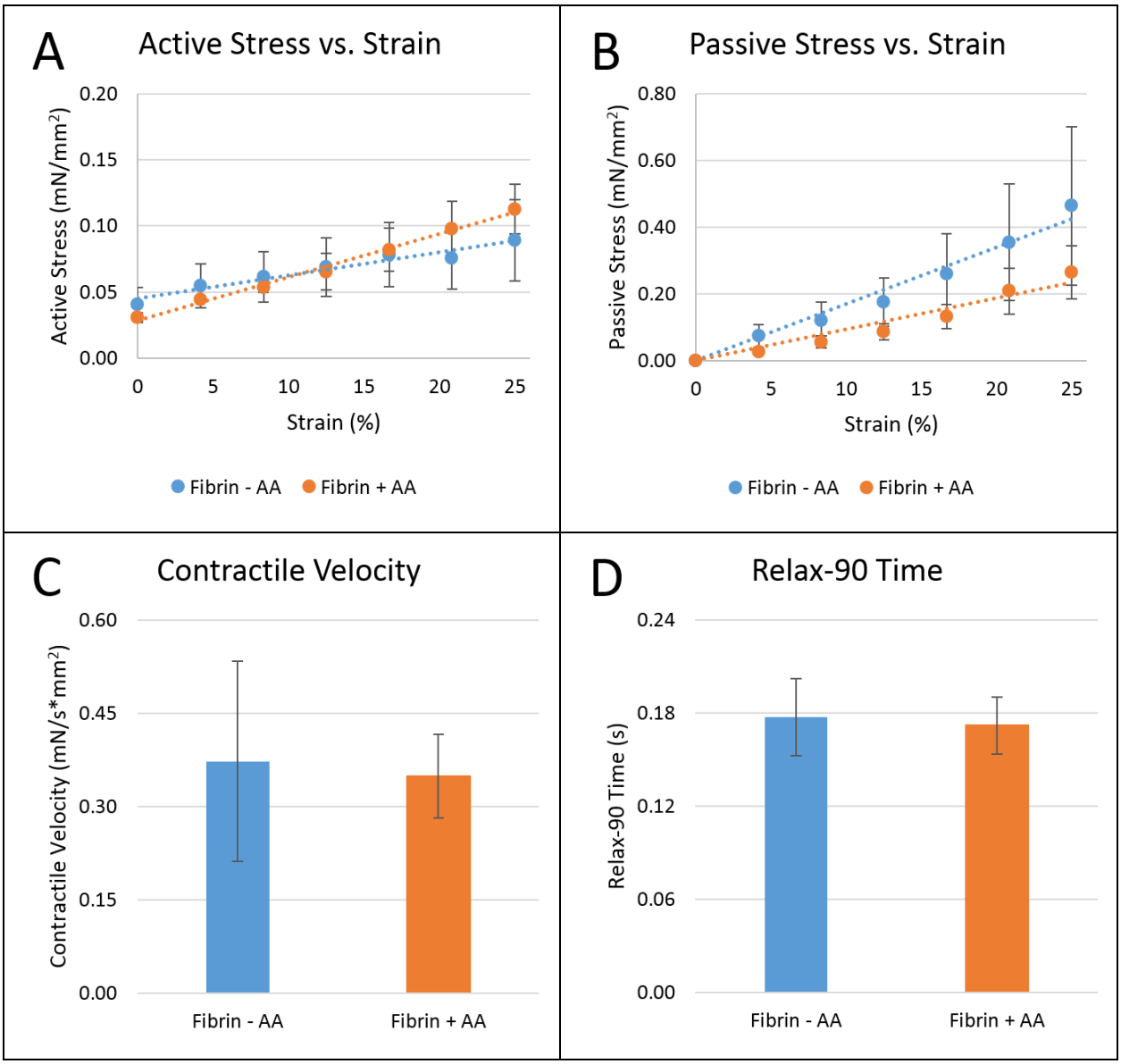

Figure 13: Contractility of fibrin tissues treated with or without ascorbic acid (AA) treatment. Panel A: Active stress vs. strain curves for fibrin tissues treated without AA ($y = 0.0017x + 0.0451$, $R^2=0.9498$) and with AA ($y=0.0033x+0.0285$, $R^2=0.9921$). Panel B: Passive stress vs. strain curves for fibrin-AA ($y=0.0169x$, $R^2=0.9748$) and fibrin+AA ($y=0.0094x$, $R^2=0.9407$). Panel C: Contractile velocity for fibrin-AA and fibrin+AA tissues. Panel D: Time to 90% relaxation of contraction for fibrin-AA and fibrin+AA tissues. All error bars are ± SEM.

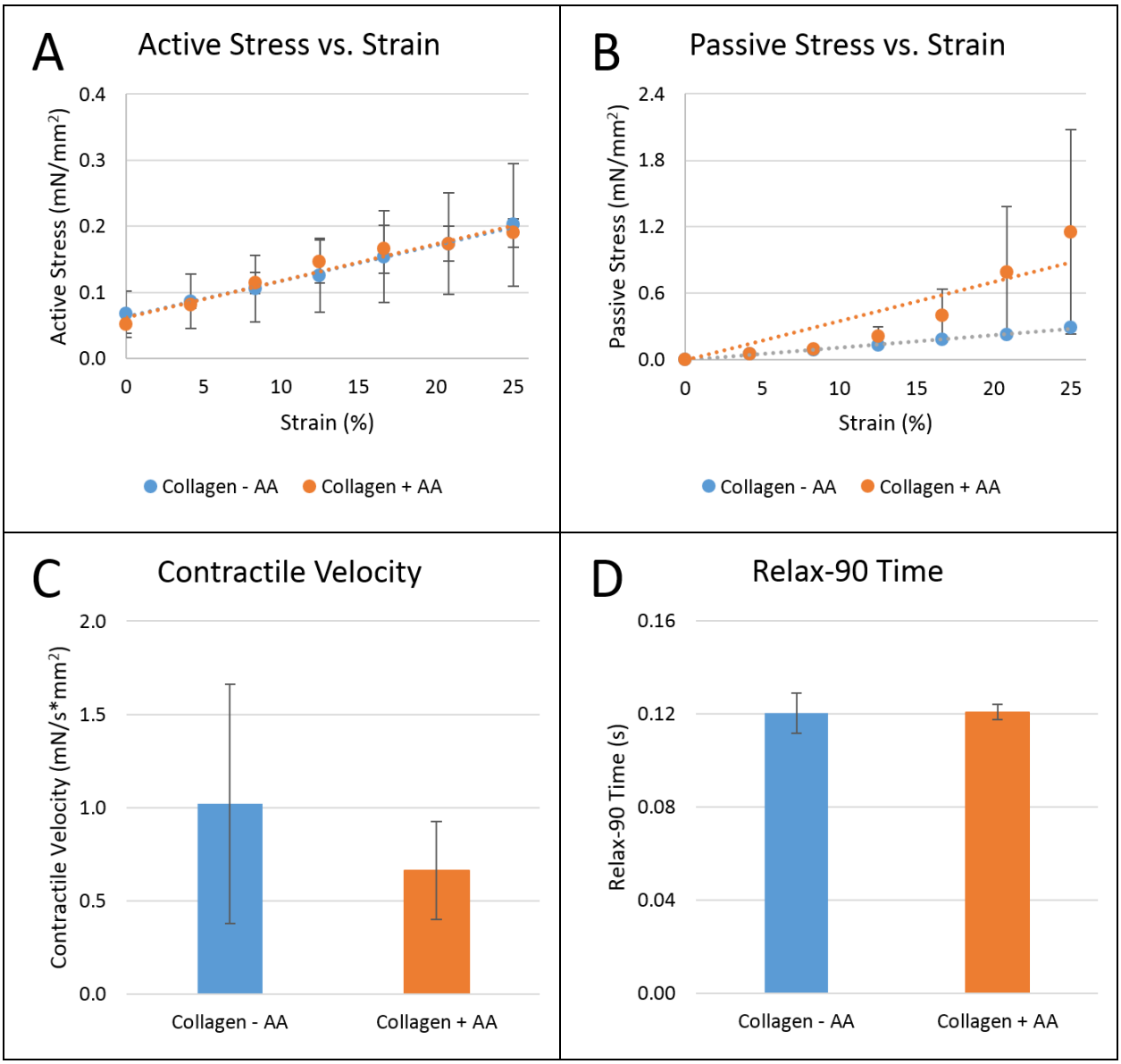

Figure 14: Contractility of collagen tissues treated with or without ascorbic acid (AA) treatment. Panel A: Active stress vs. strain curves for collagen tissues treated without AA (y = 0.0054x+0.0633, R^2=0.9954) and with AA (y=0.0056x+0.0618, R^2=0.9593). Panel B: Passive stress vs. strain curves for collagen-AA (y=0.0112x, R^2=0.9945) and collagen+AA (y=0.0353x, R^2=0.8116). Panel C: Contractile velocity for collagen-AA and collagen+AA tissues. Panel D: Time to 90% relaxation of contraction for collagen-AA and collagen+AA tissues. All error bars are ± SEM.

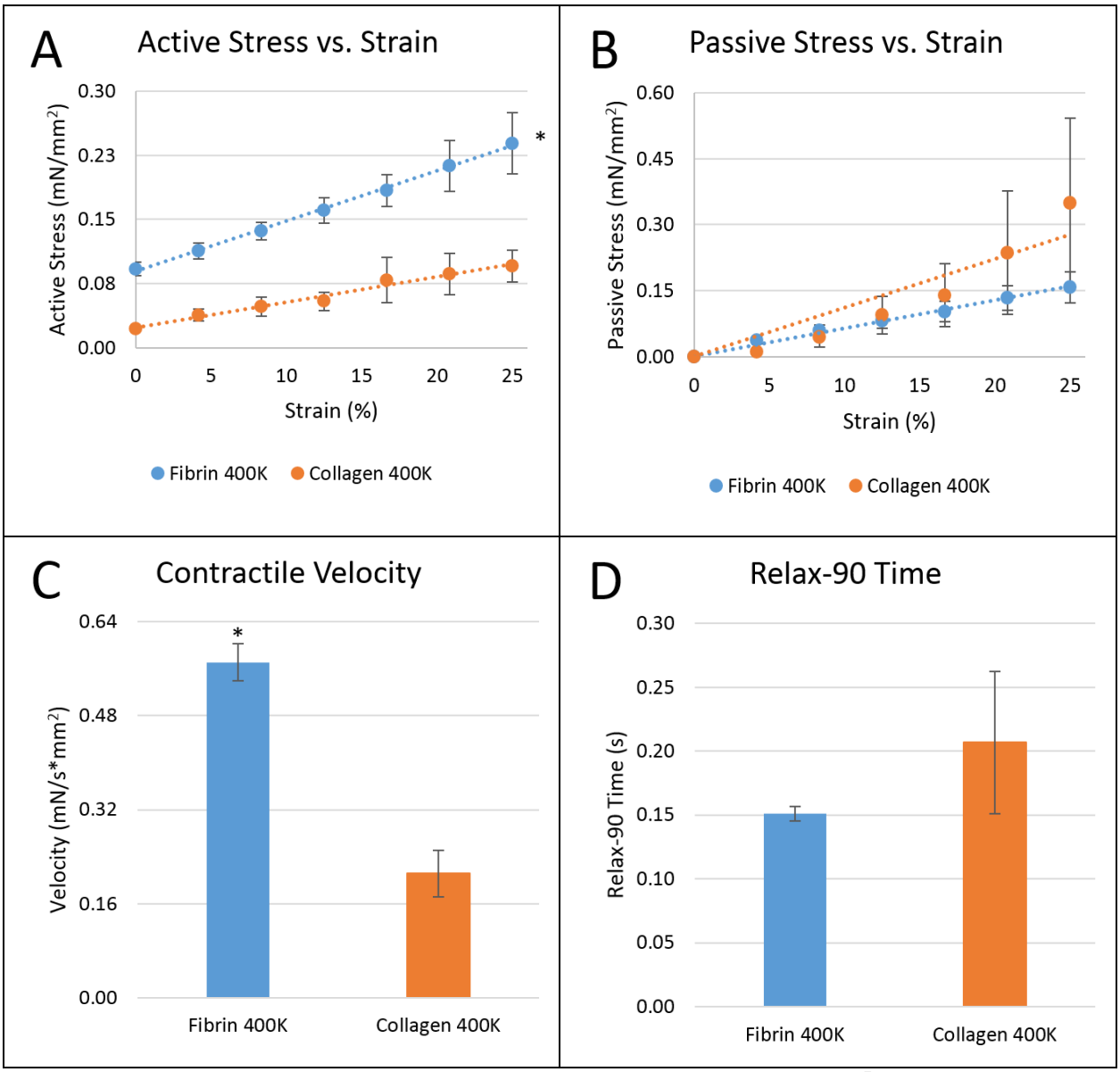

Figure 15: Contractility of collagen and fibrin tissues seeded with 4×10^5 cardiomyocytes and 4×10^4 HS-27a cells per tissue. Panel A: Active stress vs. strain curves for fibrin tissues seeded with 4×10^5 cardiomyocytes ($y = 0.0059x + 0.0891$, $R^2=0.9979$) and collagen tissues seeded with 4×10^5 cardiomyocytes ($y=0.0030x+0.0235$, $R^2=0.9805$). The average active force for fibrin-400K tissues is 2.7-fold higher than collagen-400K ($p<0.05$). Panel B: Passive stress vs. strain curves for fibrin-400K ($y=0.0064x$, $R^2=0.9907$) and collagen-400K ($y=0.0111x$, $R^2=0.8721$). Panel C: Contractile velocity for fibrin-400K and collagen-400K tissues, with fibrin-400K tissues having a 2.7-fold greater contractile velocity than collagen-400K ($p<0.05$). Panel D: Time to 90% relaxation of contraction for fibrin-400K and collagen-400K tissues. All error bars are ± SEM.

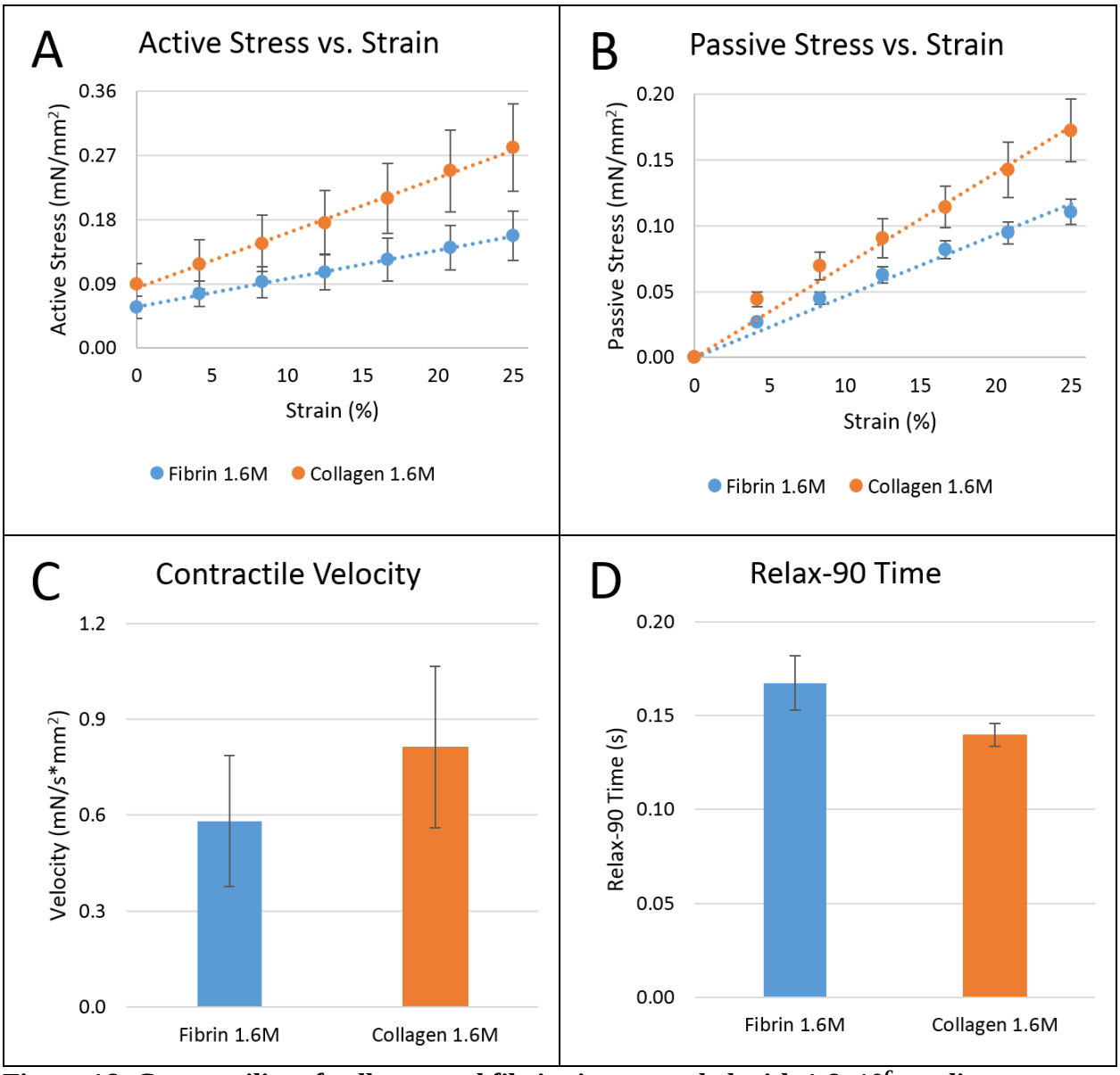

Figure 16: Contractility of collagen and fibrin tissues seeded with 1.6×10^6 cardiomyocytes and 1.6×10^5 HS-27a per tissue. Panel A: Active stress vs. strain curves for fibrin tissues seeded with 1.6×10^6 cardiomyocytes ($y = 0.0040x + 0.0583$, $R^2=0.9993$) and collagen tissues seeded with 1.6×10^6 cardiomyocytes ($y=0.0077x+0.0848$, $R^2=0.9969$). Panel B: Passive stress vs. strain curves for fibrin-1.6M ($y=0.0047x$, $R^2=0.9815$) and collagen-1.6M ($y=0.0007x$, $R^2=0.9818$). Panel C: Contractile velocity for fibrin-1.6M and collagen-1.6M tissues. Panel D: Time to 90% relaxation of contraction for fibrin-1.6M and collagen-1.6M tissues. All error bars are ± SEM.

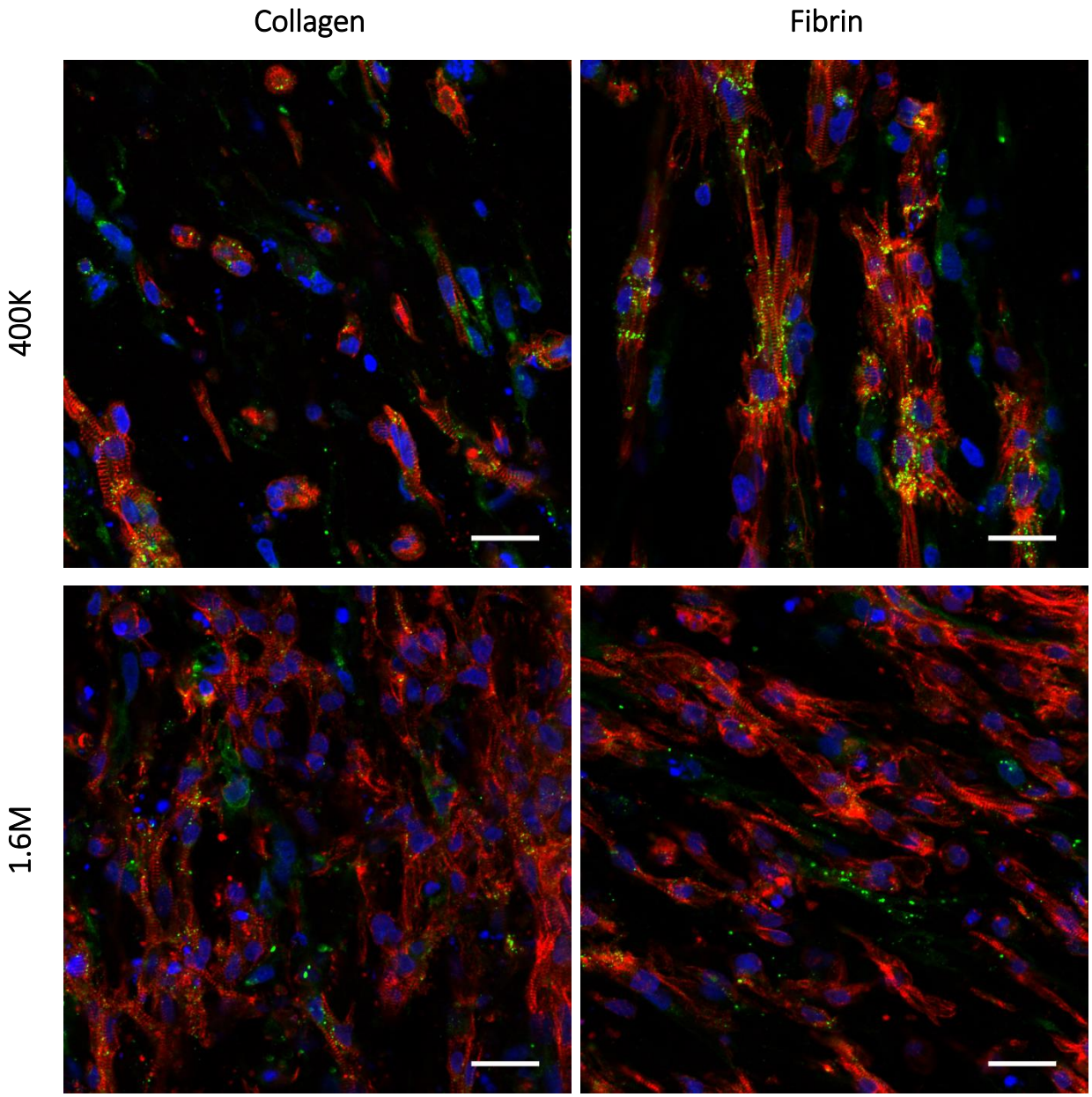

Figure 17: Immunohistochemistry of collagen and fibrin constructs. Constructs were stained for α-actinin (red), connexin-43 (green), and nuclei (blue). Constructs seeded with 1.6×10^6 cardiomyocytes (lower two panels) appear denser in cell concentration than those seeded with 4×10^5 cardiomyocytes (upper two panels). Fibrin constructs (right two panels) appear to have longer cardiomyocytes than collagen constructs (left two panels) appear to have (scale = 50μm).

Table 1: Converting uniformly distributed load to equivalent LVES-BP.

Magnet Distance	Uniformly Distributed Magnet Load (ω)	Tissue Stress	LVES-BP
cm	mN/m	kPa	mmHg
0	73	1.9	8.2
1	32	0.8	3.6
2	10	0.3	1.1
3	2	0.1	0.2

Uniformly distributed load is converted to tissue stress by taking the product of load and post length (0.5 mm) and dividing by a sample tissue cross-sectional area (0.196 mm^2). Tissue stress is then converted to left ventricular end systolic blood pressure (LVES-BP) using Lamé's equation for wall tension and pressure of a spherical chamber, assuming a chamber radius of 0.25 cm and a thickness of 0.30 cm from literature[69,70].

Table 2: LVES tension vs. gestational age.

Gestational Age	End Systolic Inner Wall Radius[69]	End Systolic Wall Thickness[69]	Systolic Blood Pressure[70]	Midwall Circ. Tension – LaPlace	Midwall Circ. Tension - Lamé	Midwall Circ. Tension	Magnet Distance
weeks	cm	cm	mmHg	mmHg	mmHg	kPa	cm
10	0.10	0.14	28	20	17	2.3	6.9
20	0.25	0.26	38	37	34	4.5	4.6
30	0.40	0.38	49	52	48	6.4	3.5
40	0.55	0.50	60	66	61	8.2	2.7
-	-	-	139	-	-	-	0

Circumferential tension at the midwall was computed via the Law of Laplace modelling tension and pressure for a spherical chamber, and Lamé's variation of the equation used when the ratio of radius to thickness is less than ten. In order to compute the magnet distance required to generate the resistive tension, midwall circumferential tension was multiplied by a sample tissue cross-sectional area of 0.196 mm^2 to get units of force, and magnet distance was back calculated using the fitted equation for force vs. magnet distance: $force(\mu N)=3720e^{-0.303x}$. The corresponding LVES-BP at a magnet distance of 0 cm is 138.9 mmHg.

References

1. WHO | Cardiovascular diseases (CVDs). *WHO* at <http://www.who.int/mediacentre/factsheets/fs317/en/>
2. Mozaffarian, D. *et al.* Heart Disease and Stroke Statistics—2015 Update A Report From the American Heart Association. *Circulation* **131,** e29–e322 (2015).
3. Heidenreich, P. A. *et al.* Forecasting the Future of Cardiovascular Disease in the United States A Policy Statement From the American Heart Association. *Circulation* **123,** 933–944 (2011).
4. Hennekens, C. H. Increasing Burden of Cardiovascular Disease Current Knowledge and Future Directions for Research on Risk Factors. *Circulation* **97,** 1095–1102 (1998).
5. Barnes, A. S. Obesity and Sedentary Lifestyles. *Tex. Heart Inst. J.* **39,** 224–227 (2012).
6. Warren, T. Y. *et al.* Sedentary Behaviors Increase Risk of Cardiovascular Disease Mortality in Men. *Med. Sci. Sports Exerc.* **42,** 879–885 (2010).
7. Acute Myocardial Infarction. at <http://www.clevelandclinicmeded.com/medicalpubs/diseasemanagement/cardiology/acute-myocardial-infarction/Default.htm>
8. Simon, H.-G. Salamanders and fish can regenerate lost structures - why can't we? *BMC Biol.* **10,** 15 (2012).
9. Kikuchi, K. & Poss, K. D. Cardiac Regenerative Capacity and Mechanisms. *Annu. Rev. Cell Dev. Biol.* **28,** 719–741 (2012).
10. French, B. A. & Kramer, C. M. Mechanisms of Post-Infarct Left Ventricular Remodeling. *Drug Discov. Today Dis. Mech.* **4,** 185–196 (2007).

11. Firth, B. G. & Dunnmon, P. M. Left ventricular dilatation and failure post-myocardial infarction: pathophysiology and possible pharmacologic interventions. *Cardiovasc. Drugs Ther. Spons. Int. Soc. Cardiovasc. Pharmacother.* **4,** 1363–1374 (1990).
12. Friedrich, E. B. & Böhm, M. Management of end stage heart failure. *Heart* **93,** 626–631 (2007).
13. Adler, E. D., Goldfinger, J. Z., Kalman, J., Park, M. E. & Meier, D. E. Palliative Care in the Treatment of Advanced Heart Failure. *Circulation* **120,** 2597–2606 (2009).
14. Costanzo, M. R. *et al.* Selection and Treatment of Candidates for Heart Transplantation A Statement for Health Professionals From the Committee on Heart Failure and Cardiac Transplantation of the Council on Clinical Cardiology, American Heart Association. *Circulation* **92,** 3593–3612 (1995).
15. Qian, L. *et al.* In vivo reprogramming of murine cardiac fibroblasts into induced cardiomyocytes. *Nature* **485,** 593–598 (2012).
16. de Carvalho, A. C. C. & Carvalho, A. B. Turning scar into muscle. *World J. Cardiol.* **4,** 267–270 (2012).
17. Riley, P. R. Converting Scar to Muscle in the Injured Heart. *Mol. Ther.* **20,** 1294–1296 (2012).
18. Gerbin, K. A. & Murry, C. E. The winding road to regenerating the human heart. *Cardiovasc. Pathol.* **24,** 133–140 (2015).
19. Doppler, S. A., Deutsch, M.-A., Lange, R. & Krane, M. Cardiac regeneration: current therapies—future concepts. *J. Thorac. Dis.* **5,** 683–697 (2013).
20. Chong, J. J. H. *et al.* Human embryonic-stem-cell-derived cardiomyocytes regenerate non-human primate hearts. *Nature* **510,** 273–277 (2014).

21. van Laake, L. W. *et al.* Human embryonic stem cell-derived cardiomyocytes survive and mature in the mouse heart and transiently improve function after myocardial infarction. *Stem Cell Res.* **1,** 9–24 (2007).

22. Caspi, O. *et al.* Transplantation of Human Embryonic Stem Cell-Derived Cardiomyocytes Improves Myocardial Performance in Infarcted Rat Hearts. *J. Am. Coll. Cardiol.* **50,** 1884–1893 (2007).

23. Laflamme, M. A. *et al.* Cardiomyocytes derived from human embryonic stem cells in pro-survival factors enhance function of infarcted rat hearts. *Nat. Biotechnol.* **25,** 1015–1024 (2007).

24. Hirt, M. N., Hansen, A. & Eschenhagen, T. Cardiac Tissue Engineering State of the Art. *Circ. Res.* **114,** 354–367 (2014).

25. Schaaf, S. *et al.* Human Engineered Heart Tissue as a Versatile Tool in Basic Research and Preclinical Toxicology. *PLoS ONE* **6,** (2011).

26. Tulloch, N. L. *et al.* Growth of Engineered Human Myocardium with Mechanical Loading and Vascular Co-culture. *Circ. Res.* **109,** 47–59 (2011).

27. Zhang, D. *et al.* Tissue-engineered cardiac patch for advanced functional maturation of human ESC-derived cardiomyocytes. *Biomaterials* **34,** 5813–5820 (2013).

28. van der Velden, J. *et al.* Force production in mechanically isolated cardiac myocytes from human ventricular muscle tissue. *Cardiovasc. Res.* **38,** 414–423 (1998).

29. Kaully, T., Kaufman-Francis, K., Lesman, A. & Levenberg, S. Vascularization—The Conduit to Viable Engineered Tissues. *Tissue Eng. Part B Rev.* **15,** 159–169 (2009).

30. Stevens, K. R., Pabon, L., Muskheli, V. & Murry, C. E. Scaffold-Free Human Cardiac Tissue Patch Created from Embryonic Stem Cells. *Tissue Eng. Part A* **15,** 1211–1222 (2009).

31. Liau, B., Zhang, D. & Bursac, N. Functional cardiac tissue engineering. *Regen. Med.* **7,** 187–206 (2012).

32. Fink, C. *et al.* Chronic stretch of engineered heart tissue induces hypertrophy and functional improvement. *FASEB J.* **14,** 669–679 (2000).

33. Zimmermann, W.-H. *et al.* Tissue Engineering of a Differentiated Cardiac Muscle Construct. *Circ. Res.* **90,** 223–230 (2002).

34. SHIMKO, V. F. & CLAYCOMB, W. C. Effect of Mechanical Loading on Three-Dimensional Cultures of Embryonic Stem Cell-Derived Cardiomyocytes. *Tissue Eng. Part A* **14,** 49–58 (2008).

35. Clause, K. C., Tinney, J. P., Liu, L. J., Keller, B. B. & Tobita, K. Engineered Early Embryonic Cardiac Tissue Increases Cardiomyocyte Proliferation by Cyclic Mechanical Stretch via p38-MAP Kinase Phosphorylation. *Tissue Eng. Part A* **15,** 1373–1380 (2009).

36. Chan, Y.-C. *et al.* Electrical stimulation promotes maturation of cardiomyocytes derived from human embryonic stem cells. *J Cardiovasc. Transl. Res.* **6,** 989–999 (2013).

37. Földes, G. *et al.* Modulation of human embryonic stem cell-derived cardiomyocyte growth: a testbed for studying human cardiac hypertrophy? *J. Mol. Cell. Cardiol.* **50,** 367–376 (2011).

38. Yang, X. *et al.* Tri-iodo-l-thyronine promotes the maturation of human cardiomyocytes-derived from induced pluripotent stem cells. *J. Mol. Cell. Cardiol.* **72,** 296–304 (2014).

39. McDevitt, T. C., Laflamme, M. A. & Murry, C. E. Proliferation of cardiomyocytes derived from human embryonic stem cells is mediated via the IGF/PI 3-kinase/Akt signaling pathway. *J. Mol. Cell. Cardiol.* **39,** 865–873 (2005).

40. Kensah, G. *et al.* Murine and human pluripotent stem cell-derived cardiac bodies form contractile myocardial tissue in vitro. *Eur. Heart J.* **34,** 1134–1146 (2013).

41. Zhang, J.-Y., Doll, B. A., Beckman, E. J. & Hollinger, J. O. Three-Dimensional Biocompatible Ascorbic Acid-Containing Scaffold for Bone Tissue Engineering. *Tissue Eng.* **9,** 1143–1157 (2003).

42. Fu, J.-D. *et al.* Distinct Roles of MicroRNA-1 and -499 in Ventricular Specification and Functional Maturation of Human Embryonic Stem Cell-Derived Cardiomyocytes. *PLoS ONE* **6,** e27417 (2011).

43. Ruan, J.-L. *et al.* Mechanical Stress Promotes Maturation of Human Myocardium From Pluripotent Stem Cell-Derived Progenitors. *STEM CELLS* **33,** 2148–2157 (2015).

44. Zimmermann, W.-H. *et al.* Engineered heart tissue grafts improve systolic and diastolic function in infarcted rat hearts. *Nat. Med.* **12,** 452–458 (2006).

45. Hirt, M. N. *et al.* Increased afterload induces pathological cardiac hypertrophy: a new in vitro model. *Basic Res. Cardiol.* **107,** (2012).

46. Schaaf, S. *et al.* Generation of strip-format fibrin-based engineered heart tissue (EHT). *Methods Mol. Biol. Clifton NJ* **1181,** 121–129 (2014).

47. Metallo, C., Azarin, S., Ji, L., De Pablo, J. & Palecek, S. Engineering tissue from human embryonic stem cells. *J. Cell. Mol. Med.* **12,** 709–729 (2008).

48. Mummery, C. L. *et al.* Differentiation of Human ES and iPS Cells to Cardiomyocytes: A Methods Overview. *Circ. Res.* **111,** 344–358 (2012).

49. Chow, M. Z., Boheler, K. R. & Li, R. A. Human pluripotent stem cell-derived cardiomyocytes for heart regeneration, drug discovery and disease modeling: from the genetic, epigenetic, and tissue modeling perspectives. *Stem Cell Res. Ther.* **4,** 97 (2013).

50. Eder, A., Vollert, I., Hansen, A. & Eschenhagen, T. Human engineered heart tissue as a model system for drug testing. *Adv. Drug Deliv. Rev.* doi:10.1016/j.addr.2015.05.010

51. Mihic, A. *et al.* The effect of cyclic stretch on maturation and 3D tissue formation of human embryonic stem cell-derived cardiomyocytes. *Biomaterials* **35,** 2798–2808 (2014).

52. Zimmer, H.-G. Who Discovered the Frank-Starling Mechanism? *Physiology* **17,** 181–184 (2002).

53. Grossman, W., Jones, D. & McLaurin, L. P. Wall stress and patterns of hypertrophy in the human left ventricle. *J. Clin. Invest.* **56,** 56–64 (1975).

54. Vincent, J.-L. Understanding cardiac output. *Crit. Care* **12,** 174 (2008).

55. Mihl, C., Dassen, W. R. M. & Kuipers, H. Cardiac remodelling: concentric versus eccentric hypertrophy in strength and endurance athletes. *Neth. Heart J.* **16,** 129–133 (2008).

56. Kahan, T. & Bergfeldt, L. Left ventricular hypertrophy in hypertension: its arrhythmogenic potential. *Heart* **91,** 250–256 (2005).

57. de Vroomen, M., Cardozo, R. H., Steendijk, P., van Bel, F. & Baan, J. Improved contractile performance of right ventricle in response to increased RV afterload in newborn lamb. *Am. J. Physiol. Heart Circ. Physiol.* **278,** H100–105 (2000).

58. Klautz, R. J., Teitel, D. F., Steendijk, P., van Bel, F. & Baan, J. Interaction between afterload and contractility in the newborn heart: evidence of homeometric autoregulation in the intact circulation. *J. Am. Coll. Cardiol.* **25,** 1428–1435 (1995).

59. Rodriguez, A. G., Han, S. J., Regnier, M. & Sniadecki, N. J. Substrate Stiffness Increases Twitch Power of Neonatal Cardiomyocytes in Correlation with Changes in Myofibril Structure and Intracellular Calcium. *Biophys. J.* **101,** 2455–2464 (2011).

60. Raub, C. B., Putnam, A. J., Tromberg, B. J. & George, S. C. Predicting bulk mechanical properties of cellularized collagen gels using multiphoton microscopy. *Acta Biomater.* **6,** 4657–4665 (2010).

61. Bashey, R. I., Martinez-Hernandez, A. & Jimenez, S. A. Isolation, characterization, and localization of cardiac collagen type VI. Associations with other extracellular matrix components. *Circ. Res.* **70,** 1006–1017 (1992).

62. Berg, J. M., Tymoczko, J. L. & Stryer, L. Regulatory Strategies: Enzymes and Hemoglobin. (2002). at <http://www.ncbi.nlm.nih.gov/books/NBK21158/>

63. Thomson, K. S. *et al.* Prevascularized microtemplated fibrin scaffolds for cardiac tissue engineering applications. *Tissue Eng. Part A* **19,** 967–977 (2013).

64. Duong, H., Wu, B. & Tawil, B. Modulation of 3D fibrin matrix stiffness by intrinsic fibrinogen-thrombin compositions and by extrinsic cellular activity. *Tissue Eng. Part A* **15,** 1865–1876 (2009).

65. Jockenhoevel, S. *et al.* Fibrin gel -- advantages of a new scaffold in cardiovascular tissue engineering. *Eur. J. Cardio-Thorac. Surg. Off. J. Eur. Assoc. Cardio-Thorac. Surg.* **19,** 424–430 (2001).

66. Du, J., Cullen, J. J. & Buettner, G. R. Ascorbic acid: Chemistry, biology and the treatment of cancer. *Biochim. Biophys. Acta* **1826,** 443–457 (2012).

67. Wang, Z., Volinsky, A. A. & Gallant, N. D. Crosslinking effect on polydimethylsiloxane elastic modulus measured by custom-built compression instrument. *J. Appl. Polym. Sci.* **131,** n/a–n/a (2014).

68. *Biophysical Methods in Cell Biology*. (Academic Press, 2015).

69. Sutton, M. G. S. J. *et al.* Quantitative assessment of growth and function of the cardiac chambers in the normal human fetus: a prospective longitudinal echocardiographic study. *Circulation* **69,** 645–654 (1984).

70. Struijk, P. C. *et al.* Blood pressure estimation in the human fetal descending aorta. *Ultrasound Obstet. Gynecol.* **32,** 673–681 (2008).

71. Sniadecki, N. J. & Chen, C. S. Microfabricated silicone elastomeric post arrays for measuring traction forces of adherent cells. *Methods Cell Biol.* **83,** 313–328 (2007).

72. Guterl, K. A., Haggart, C. R., Janssen, P. M. & Holmes, J. W. Isometric contraction induces rapid myocyte remodeling in cultured rat right ventricular papillary muscles. *Am. J. Physiol. - Heart Circ. Physiol.* **293,** H3707–H3712 (2007).

73. Russell, B., Curtis, M. W., Koshman, Y. E. & Samarel, A. M. Mechanical stress-induced sarcomere assembly for cardiac muscle growth in length and width. *J. Mol. Cell. Cardiol.* **48,** 817–823 (2010).

74. Kerckhoffs, R. C. P., Omens, J. & McCulloch, A. D. A single strain-based growth law predicts concentric and eccentric cardiac growth during pressure and volume overload. *Mech. Res. Commun.* **42,** 40–50 (2012).

75. Gopalan, S. M. *et al.* Anisotropic stretch-induced hypertrophy in neonatal ventricular myocytes micropatterned on deformable elastomers. *Biotechnol. Bioeng.* **81,** 578–587 (2003).

76. Simpson, D. G., Majeski, M., Borg, T. K. & Terracio, L. Regulation of cardiac myocyte protein turnover and myofibrillar structure in vitro by specific directions of stretch. *Circ. Res.* **85,** e59–69 (1999).

77. Geiger, P. C. *et al.* Mechanisms underlying increased force generation by rat diaphragm muscle fibers during development. *J. Appl. Physiol. Bethesda Md 1985* **90,** 380–388 (2001).

78. Hamrell, B. B., Roberts, E. T., Carkin, J. L. & Delaney, C. L. Myocyte morphology of free wall trabeculae in right ventricular pressure overload hypertrophy in rabbits. *J. Mol. Cell. Cardiol.* **18,** 127–138 (1986).

79. Narici, M. V. & Maganaris, C. N. Adaptability of elderly human muscles and tendons to increased loading. *J. Anat.* **208,** 433–443 (2006).

80. Reconditi, M. *et al.* Sarcomere-length dependence of myosin filament structure in skeletal muscle fibres of the frog. *J. Physiol.* **592,** 1119–1137 (2014).

81. Mansour, H., de Tombe, P. P., Samarel, A. M. & Russell, B. Restoration of resting sarcomere length after uniaxial static strain is regulated by protein kinase Cepsilon and focal adhesion kinase. *Circ. Res.* **94,** 642–649 (2004).

82. Rosenblat, G. *et al.* Acylated ascorbate stimulates collagen synthesis in cultured human foreskin fibroblasts at lower doses than does ascorbic acid. *Connect. Tissue Res.* **37,** 303–311 (1998).

83. Choi, K.-M. *et al.* Effect of ascorbic acid on bone marrow-derived mesenchymal stem cell proliferation and differentiation. *J. Biosci. Bioeng.* **105,** 586–594 (2008).

84. K&J Magnetics Blog. at <https://www.kjmagnetics.com/blog.asp?p=temperature-and-neodymium-magnets>